

Development and Testing of Instrumentation for UAV-Based Flux Measurements within Terrestrial and Marine Atmospheric Boundary Layers

BENJAMIN D. REINEMAN

Scripps Institution of Oceanography, and Department of Mechanical and Aerospace Engineering, University of California, San Diego, La Jolla, California

LUC LENAIN, NICHOLAS M. STATOM, AND W. KENDALL MELVILLE

Scripps Institution of Oceanography, University of California, San Diego, La Jolla, California

(Manuscript received 16 August 2012, in final form 7 January 2013)

ABSTRACT

Instrumentation packages have been developed for small (18–28 kg) unmanned aerial vehicles (UAVs) to measure momentum fluxes as well as latent, sensible, and radiative heat fluxes in the atmospheric boundary layer (ABL) and the topography below. Fast-response turbulence, hygrometer, and temperature probes permit turbulent momentum and heat flux measurements, and shortwave and longwave radiometers allow the determination of net radiation, surface temperature, and albedo. UAVs flying in vertical formation allow the direct measurement of fluxes within the ABL and, with onboard high-resolution visible and infrared video and laser altimetry, simultaneous observation of surface topography or ocean surface waves. The low altitude required for accurate flux measurements (typically assumed to be 30 m) is below the typical safety limit of manned research aircraft; however, with advances in laser altimeters, small-aircraft flight control, and real-time kinematic differential GPS, low-altitude flight is now within the capability of small UAV platforms. Flight tests of instrumented BAE Systems Manta C1 UAVs over land were conducted in January 2011 at McMillan Airfield (Camp Roberts, California). Flight tests of similarly instrumented Boeing Insitu ScanEagle UAVs were conducted in April 2012 at the Naval Surface Warfare Center, Dahlgren Division (Dahlgren, Virginia), where the first known measurements of water vapor, heat, and momentum fluxes were made from low-altitude (down to 30 m) UAV flights over water (Potomac River). This study presents a description of the instrumentation, summarizes results from flight tests, and discusses potential applications of these UAVs for (marine) atmospheric boundary layer studies.

1. Introduction

Current global momentum and heat flux products are insufficiently validated, especially at high latitudes and in extreme conditions (Curry et al. 2004; Bourassa et al. 2013; Brunke et al. 2011). A fundamental goal in air–sea interaction research is to refine the parameterizations used by satellite-derived products with direct in situ measurements of atmospheric state and momentum and energy fluxes. The most reliable direct atmospheric measurements of air–sea fluxes are made at low altitudes within the so-called constant flux layer in the first few tens of

meters of the marine atmospheric boundary layer (MABL; Jones and Toba 2001). Shipboard measurements are affected by flow distortion around the vessel (see, e.g., Yelland et al. 1998; Edson et al. 1998; Bradley and Fairall 2006). Deep-water moorings, such as the Air–Sea Interaction Spar (ASIS) buoy developed by Graber et al. (2000), have been used for air–sea flux measurements (Martz et al. 2009), but the cost and risk of deployment and recovery can be substantial, especially in high wind and wave environments (Bourassa et al. 2013), limiting their use. Arguably, the most reliable flux measurements in the open ocean are performed from the very stable R/P *FLIP* (*Floating Instrument Platform*; e.g., Jones and Toba 2001; Grachev et al. 2003). Ship, platform, and buoy measurements, however, cannot capture the spatial evolution of ocean surface features, winds, and fluxes without expensive replication of instrument packages and platforms.

Corresponding author address: Benjamin D. Reineman, Scripps Institution of Oceanography, University of California, San Diego, 9500 Gilman Dr., La Jolla, CA 92093-0213.
E-mail: reineman@ucsd.edu

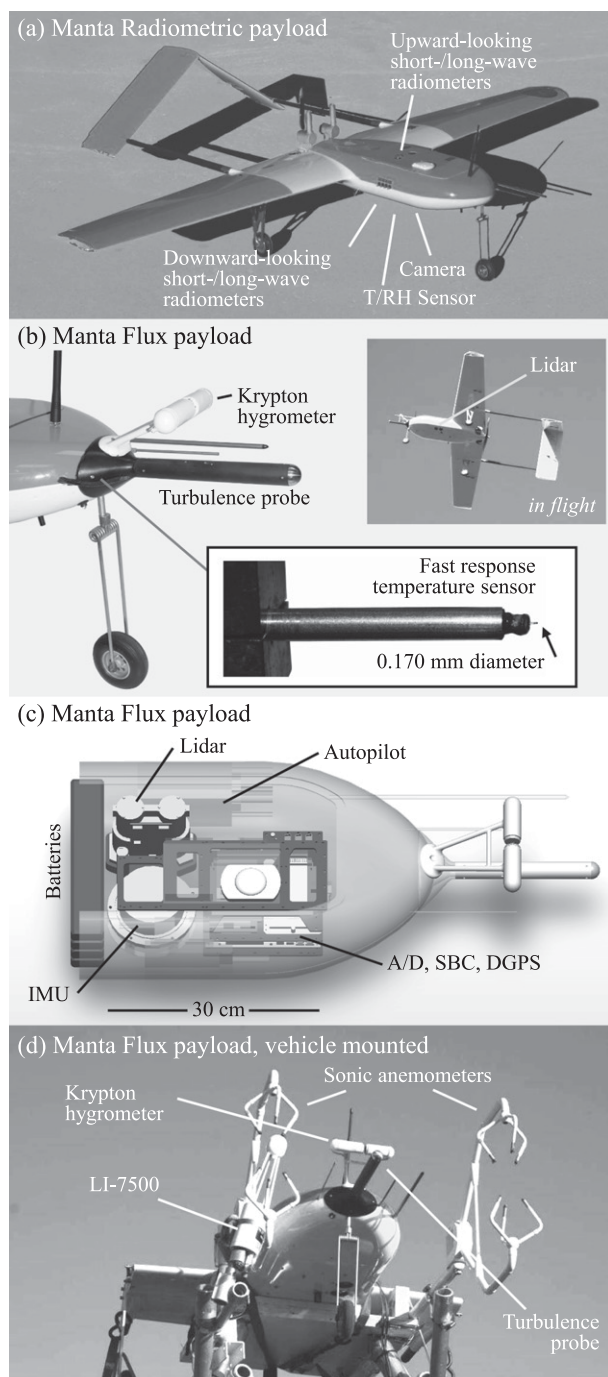


FIG. 1. BAE Systems Manta C1s instrumented for atmospheric boundary layer measurements. (a) Manta with Radiometric payload for image acquisition and measurements of radiation flux, and (b) Manta with Flux payload (close-up view of nose instrumentation) for measurements of mean wind, turbulence, momentum and heat flux, and surface elevation. Insets show the Manta in flight and a close-up view of the temperature sensor. (c) Computer graphic showing the Flux payload, which includes analog-to-digital (A/D) circuitry and SBC. (d) Manta fuselage with Flux payload mounted on a pickup truck for comparison measurements of wind and water vapor (see section 3b) with two sonic anemometers (Campbell Scientific CSAT3s) and a LI-7500 open-path gas analyzer (LI-COR).

The estimation of atmospheric fluxes by direct measurement of turbulent quantities (wind velocities, water vapor, and temperature) from aircraft has been an emerging field in recent decades. Airborne measurements have the advantage of being able to survey large areas in a relatively short amount of time, and, over the ocean, can complement ship- and platform-based measurements of surface and subsurface phenomena having a surface signature (e.g., Webster and Lukas 1992; Marmorino et al. 2010). Airborne observations of the turbulent wind generally proceed from determination of the relative wind using differential pressure measurements from an array of ports on the nose (radome) of an aircraft (e.g., Brown et al. 1983; Khelif et al. 1999; Kalogiros and Wang 2002), or protruding on a probe [e.g., National Oceanic and Atmospheric Administration (NOAA)'s Best Atmospheric Turbulence (BAT) probe; see Crawford and Dobosy 1992]. Earth-referenced wind is then determined using velocity and attitude information provided by GPS and an inertial measurement unit (IMU), as discussed in detail in the following sections. Accurate measurements of both the relative wind and the platform motion and orientation are essential for accurate wind and therefore accurate flux measurements. Bange and Roth (1999) developed a portable "Helipod" system, which is tethered to a helicopter and capable of performing low-altitude flux measurements. Holder et al. (2011) demonstrated low-altitude flux measurements using instruments mounted directly to a helicopter, held in front of the rotor downwash. Petersen and Renfrew (2009) recently demonstrated turbulence measurements in a mid-size passenger jet flying at low altitudes over the North Atlantic, using a five-port array on the aircraft radome.

Interest in unmanned platforms for atmospheric research has been growing, especially in situations too remote or dangerous for manned aircraft. Over a dozen previous unmanned aerial vehicle (UAV)-based atmospheric experiments are conveniently tabulated by Houston et al. (2012), who also describe current airspace regulations. As suggested by Bourassa et al. (2013), unmanned aircraft platforms will have an important role in acquiring near-surface atmospheric flux measurements, especially in high-latitude and extreme conditions, where current air-sea flux parameterizations and satellite-derived flux products are unreliable.

In the 1990s, Valero et al. (1996) flew a UAV equipped with shortwave and longwave radiometers to determine radiometric flux. Aerosonde UAVs (Aerosonde Pty Ltd., Notting Hill, Victoria, Australia) have been used for meteorological research for over a decade, including flights into tropical cyclones since 2005 (Cascella et al. 2008; Lin and Lee 2008) and in high winds in the Antarctic (Cassano and Knuth 2010), but they have not been

instrumented for direct flux measurements. Van den Kroonenberg et al. (2008) used a five-port directional wind probe on a small electric unmanned aircraft for measuring the mean wind vector. Recently, Thomas et al. (2012) made water vapor flux measurements over the desert with an instrumented BAE Systems Manta (a model similar to one of the UAVs used in the present study).

In this paper, we describe the development and testing of UAV instrumentation packages capable of making direct flux measurements of momentum and of sensible and latent heat within the ABL while simultaneously measuring surface topography or surface wave kinematics. Two platforms are used: the BAE Systems Manta C1 (Fig. 1), a runway takeoff/landing UAV (<http://events.us.baesystems.com/SAS/prodserv/pdf/BAE-Systems-Manta.pdf>); and the Boeing Insitu ScanEagle (<http://www.insitu.com/scaneagle>), a UAV capable of ship-based launch and recovery (Fig. 2). UAV specifications and capabilities are given in Table 1. Aircraft control, for both platforms, is completely autonomous, including takeoff and landing. Pilots have the option to enable manual control (Mantas) or semimanual (ScanEagles) in an emergency situation. During flight, GPS waypoints, altitudes, ascent and descent rates, and airspeed can be prescribed by the pilot “on the fly.” The UAVs, with real-time kinematic differential GPS (RTK-DGPS) as well as, for the Mantas, feedback from laser altimetry, are able to fly below the typical safety limit of manned aircraft operations.

Several different payloads with different measurement objectives have been developed, and will be discussed in the following sections; brief descriptions are given here. For low-altitude flux measurements, payloads include turbulence probes and fast-response temperature and humidity probes for momentum, heat, and water vapor flux measurements. Careful design and testing of an accurate turbulence probe, as demonstrated in this study, are essential for the ability to measure momentum and scalar fluxes. A laser altimeter is used for instantaneous surface elevation measurement, and in the Manta, for low-altitude flight control. Higher altitude UAVs are instrumented with visible and, for the ScanEagle, infrared imaging systems, as well as upward- and downward-looking radiometers for shortwave and longwave radiation measurements. With two UAVs flown in vertical formation,¹ maintaining the lower aircraft

in the field of view of the upper UAV permits the boundary layer and surface measurements from the lower UAV to be analyzed in the context of the wide field-of-view images of features recorded by the upper aircraft.

In section 2, we describe the system instrumentation and operation as well as the turbulence probe design, georeferenced wind calculation, and uncertainty analysis. In section 3, we discuss turbulence probe calibration and system performance validation using data from wind tunnel experiments and ground-vehicle-based tests. In section 4, we present results from engineering flight tests of payloads in Manta UAVs over land (McMillan Airfield, Camp Roberts, California), including performance validation from in-flight maneuvers, flux measurements within vertical profiles, and comparisons between the UAV- and tower-based measurements. Flux measurement methodology is also detailed in this section. In section 5, we present results from flight tests of instrumented ScanEagles over water (Potomac River, Dahlgren, Virginia).

2. UAV instrumentation and operation

a. Instrumentation and acquisition

We have developed two payloads for the Mantas—“Flux” for low-altitude flux measurements and “Radiometric” for radiometric measurements—and three payloads for the ScanEagle: Flux and Radiometric are similar to the corresponding Manta payloads, and an additional “Imaging” payload for visible and infrared imaging. Table 2 summarizes which measurements are performed by the various payloads and gives weight and power specifications. Detailed sensor information, with accuracies and response times, is given in Table 3. Though acquisition electronics for the two platforms are similar, ScanEagle payloads have been miniaturized to fit within more stringent size and weight restrictions and ruggedized to withstand the high accelerations of launch (specified as up to 50 g; we measured up to 27 g) and recovery (specified as up to 20 g; the IMU was powered off for landing). The scientific payloads are designed to be isolated from the flight control systems, ensuring that any electrical or software failure in the scientific instrumentation would not jeopardize the control of the aircraft. Manta payloads are shown in Fig. 1 and ScanEagle payloads in Fig. 3. A flowchart of UAV control, data acquisition, and ground communication is presented in Fig. 4.

The Flux payloads (Manta and ScanEagle) carry a fast-response turbulence probe to measure the relative wind in three dimensions. Small commercial sensors are available for this purpose (e.g., Aeroprobe, <http://www.aeroprobe.com>), but at probe lengths required to extend

¹ This was demonstrated autonomously with the Mantas during experiments at McMillan Airfield (see section 4), and is anticipated as a semiautonomous operation for the ScanEagles in future experiments.

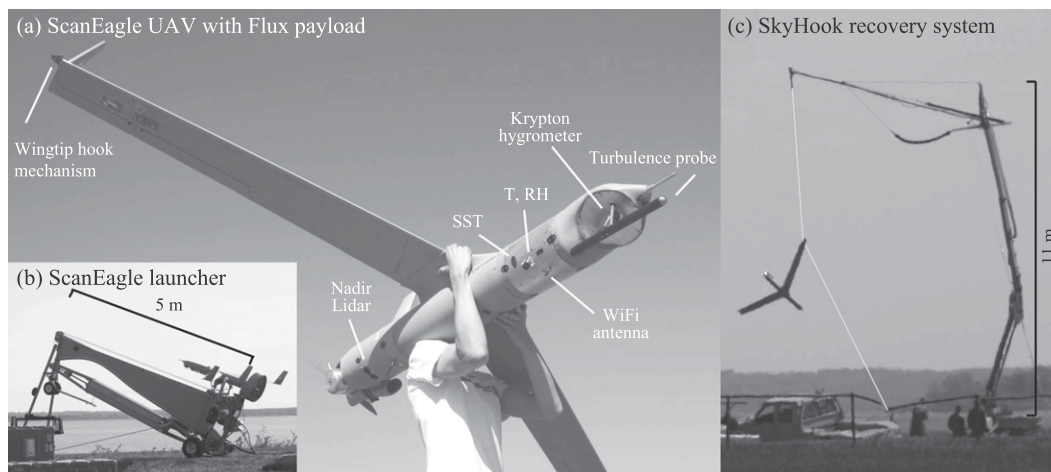


FIG. 2. Boeing Insitu ScanEagle UAV instrumented for atmospheric boundary layer measurements. (a) ScanEagle with Flux payload for measurements of mean wind, turbulence, momentum and heat flux, and surface elevation. (b) Inset shows the pneumatic launcher and (c) SkyHook recovery system shortly after ScanEagle recovery on the vertical line, which is artificially highlighted for clarity.

past the main flow distortion because of the fuselage of the UAV, they are susceptible to vibration and degraded frequency response. Well-established probes such as the Rosemount 858 (now Goodrich 0858; e.g., Khelif et al. 1999; Williams and Marcotte 2000) or BAT (e.g., Crawford and Dobosy 1992; Garman et al. 2006) are too heavy or large for the UAVs used in this study. For this application, we developed a custom precision probe in house with the goals of rigidity and fast response. The design of the probe is detailed in section 2b, the calculations for Earth-referenced wind from differential pressure measurements and attitude and velocity information are presented in section 2c, and experiments for calibration and validation are described in sections 3 and 4.

Combined with precise relative wind velocity measurements from a turbulence probe, accurate velocity and attitude measurements are essential for determining accurate momentum and scalar fluxes. To the authors' knowledge, the IMUs used in this study are the most accurate units to date to be used for airborne (manned or unmanned) direct flux measurements. The Manta Flux payload includes a Honeywell (Morristown, New Jersey) HG1700 AG58 IMU, and the ScanEagle Flux payload includes a Northrop Grumman (Falls Church, Virginia) LN200 IMU. Both Flux payloads carry a NovAtel (Calgary, Alberta, Canada) Synchronized Position Attitude Navigation (SPAN) unit, which synchronizes and couples the IMU with the DGPS. All payloads include NovAtel OEMV-3 RTK-DGPS receivers. The position, velocity,

TABLE 1. UAV specifications (ScanEagle specifications based on the "dual bay" configuration used in this study).

	BAE Systems Manta C1	Boeing Insitu ScanEagle
Mission endurance	5 h (for 6.8-kg payload)	>11 h (for 3-kg payload)
Mission airspeed	23.1–33.4 m s ⁻¹ (45–65 kt)	28.3–30.9 m s ⁻¹ (55–60 kt)
Dash airspeed	38.6 m s ⁻¹ (75 kt)	36.0 m s ⁻¹ (70 kt)
Stall airspeed	19.5 m s ⁻¹ (38 kt)	approx. 23.1 m s ⁻¹ (45 kt)
Service ceiling	5.3 km	4.9 km (19 kg takeoff weight)
Control radio range	37 km (20 nm) line of sight	100 km (54 nm) line of sight
Engine	4.0 kW (5.5 hp), two stroke/two cylinder	1.4 kW (1.9 hp), two stroke/two cylinder
Max takeoff weight	27.7 kg	22.0 kg
Fuel capacity	6.1 kg	5.6 kg
Payload capacity	6.8 kg	approx. 8.5 kg, split between fuel and payload
Payload power	User-supplied batteries	Up to 45 W (onboard generator)
Wing span	2.7 m	3.11 m
Length	1.9 m (including tail)	1.98 m
Autopilot/navigation	Cloud Cap Piccolo II	Boeing Insitu
Launch method	Rolling runway takeoff	Portable pneumatic launcher
Recovery method	Rolling runway landing	"SkyHook" wing capture with vertical line

TABLE 2. Payload measurement summary. See text for definitions of Flux, Radiometric, and Imaging payloads. Platform abbreviations are S for ScanEagle and M for Manta. Payload weight includes sensors, acquisition electronics and wiring, and aluminum framing. Instrument models and details are presented in Table 3.

Measurement	Flux	Radiometric	Imaging
UAV platform	M, S	M, S	S
Payload weight* (kg)	6.0, 3.1	5.1, 1.9	2.1
Payload power (W)	36, 33	26, 23	32
3D wind, flux measurements	Yes	No	No
Fast-response temperature, humidity	Yes	No	No
Slow-response temperature, humidity	Yes	Yes	Yes
Shortwave/longwave, up-/downwelling radiation	No	Yes	No
High-resolution nadir visible imagery	No	Yes	Yes
Infrared imagery	No	No	Yes
Nadir point lidar altimeter	Yes	No	Yes
Sea surface temperature** (S only)	Yes	Yes	Yes

* Manta payload weights include 2.0 kg of lithium-ion batteries.

** Sea surface temperature sensors are only installed in ScanEagle payloads, though they were not yet operational for the over-water flights discussed in the present study.

and orientation are refined in postprocessing using NovAtel's Waypoint Inertial Explorer. After postprocessing, estimated root-mean-squared (RMS) accuracies for the HG1700 (Manta) are 2.0 cm s^{-1} for horizontal and 1.0 cm s^{-1} for vertical velocity, 0.007° for roll and pitch, and 0.011° for yaw; estimated RMS accuracies for the LN200 (ScanEagle) are 2.0 cm s^{-1} for horizontal and 1.0 cm s^{-1} for vertical velocity, 0.005° for roll and pitch, and 0.008° for yaw (<http://www.novatel.com/span>).

The Manta and ScanEagle Flux payloads also carry a fast-response optical temperature probe (OEM-MNT with OTG-M170 sensor) from Opsens Inc. (Quebec City, Quebec, Canada). This probe makes use of the bandgap dependence on temperature of a gallium arsenide crystal to provide atmospheric temperature measurements. A comparison of temperature spectra from the optical probe and a sonic anemometer in an outdoor stationary test is shown in Fig. 5. The optical probe samples internally at 50 Hz but reaches its noise floor at about 3–5 Hz (5–9 m at cruising speed). Fast-response water vapor probes, KH20 krypton hygrometers from Campbell Scientific (Logan, Utah), were repackaged into lightweight carbon fiber mounts and affixed adjacent to the turbulence probe on the noses of these flux-measuring aircraft (see Figs. 1 and 3). Combined with the turbulence-probe-derived wind calculation, these temperature and moisture measurements are used to calculate sensible

and latent heat flux, as is described in section 4c. All payloads include Vaisala (Helsinki, Finland) HMP45C temperature (T) and relative humidity (RH) probes. For the Flux payloads, the slower-response HMP45C (stated 15-s response time) is used as a secondary source of near-zero-drift mean temperature and moisture measurement.

The increase in measured temperature resulting from the adiabatic heating of air decelerating at the sensor is given by (see, e.g., Lenschow 1986; Khelif et al. 1999)

$$\frac{T_m}{T_s} = R_f M^2 \left(\frac{\gamma - 1}{2} \right) + 1, \quad (1)$$

where T_m is the measured temperature (K), T_s is the static temperature, M is Mach number, and γ is the ratio of specific heats (≈ 1.4 for air). Recovery factor R_f is a sensor-specific factor to compensate for incomplete flow stagnation at the sensor. Because there is no self-heating in the optical sensor, we assume measured temperature equals recovered temperature (temperature of the decelerated air at the sensor). Given the small Mach number ($M \approx 0.08$), and if we assume a worst-case recovery factor of $R_f = 1$, we estimate the difference between measured and static air temperature to be less than 0.4°C (comparable to the 0.2°C absolute sensor accuracy); we have decided not to include these effects in the current analysis. Variability in measured temperature because of cruise speed variation is determined to be smaller than the resolution of the sensor (0.01°C).

Measurement Devices Ltd. (Aberdeen, Scotland) nadir-looking lidar units, mounted in the Manta Flux and ScanEagle Flux and Imaging payloads, measure distance to the surface. These pulsed laser/receiver units operate at 1 kHz and are internally averaged and output at 25 (Manta) or 44 Hz (ScanEagle). The range data are recorded by onboard solid-state drives, and on the Manta, are also filtered with a running average and supplied to the autopilot at 1 Hz. During low-level flight, the filtered range measurements provide an optional supplement to the aboveground altitude determined with DGPS and the autopilot's digital elevation model, and are used by the autopilot with more confidence the lower the altitude.

The Manta Radiometric and ScanEagle Radiometric and Imaging payloads acquire high-resolution (>1.2 megapixel) digital video data with a Prosilica (Stadtroda, Germany) GC1290 (Manta) and GC1380H (ScanEagle), enabling detailed imaging of the surface, and in the case of flights over water, quantification of ocean surface features including fronts, whitecap coverage, and wave

TABLE 3. UAV payload instrumentation, with response time (or sampling frequency for lidar, cameras, and GPS/IMU) given when available. Accuracy from the manufacturer is listed where appropriate. See section 2a for GPS/IMU accuracies. Payload abbreviations are MF and MR for Manta Flux and Radiometric payloads, respectively, and SF, SR, and SI for ScanEagle Flux, Radiometric, and Imaging payloads, respectively. Instrument details are found in section 2. Where two comma-separated values are listed either for weight or response, they refer to Manta and ScanEagle instruments, respectively.

Payload	Instrument	Weight (kg)	Response	Measurement/function (accuracy)
MF, SF	Turbulence probe ^a	0.15, 0.11	>100 Hz	Relative wind, Earth-referenced wind (see text), momentum and scalar fluxes
MF, SF	Campbell Scientific krypton hygrometer	0.14	>100 Hz	Water vapor, latent heat flux
MF, SF	Opsens fiber optic temperature sensor	0.12	3–5 Hz	Temperature (<0.2°C absolute accuracy, 0.01°C resolution), sensible heat flux
MF, SF/I	Measurement Devices Ltd nadir lidar altimeter ^b	0.90, 0.27	25, 44 Hz	Topography, surface waves (± 5 cm accuracy, 1-cm resolution) (MF only: flight control)
MR, SR	Pyrano-pyrgeometers ^c (2 times each)	Varies	Varies	Shortwave/longwave, up-/downwelling radiation, SST
MR, SR/I	Prosilica digital camera (M: GC1290, S: GC1380H)	0.19	5 Hz	Ocean surface processes, wave kinematics and breaking
SI	FLIR longwave IR camera (A325)	0.46	8.5 Hz	Ocean surface temperature structure (0.05°C noise equivalent temperature difference)
SF/R/I	Nose camera (Advance Security SSC-106CXHRB29)	0.02	—	Navigation assistance, conditions monitoring
SF/R/I	Everest Sea-Therm	0.04	2 Hz	Sea surface temperature (SST)
All	Vaisala humidity, temperature sensor (HMP45C, repackaged)	0.05	15 s	T and RH profiles (<0.2°C and <2% RH), bulk fluxes
All	NovAtel OEMV-3 RTK-DGPS	0.08	4, 1 Hz	Position, velocity (M only: aircraft control)
MF	Honeywell IMU (HG1700 AG58)	0.73	100 Hz	Georeferencing winds and lidar
SF	Northrop Grumman IMU (LN200)	0.75	200 Hz	Georeferencing winds and lidar
MF, SF	NovAtel SPAN circuitry	0.13	—	GPS/IMU synchronization
All	DAQ, electronics	1.42, 0.73	—	Acquisition, processing, power regulation, data storage

^a Custom-designed probe, using All Sensors prime-grade, amplified, temperature-compensated differential pressure sensors and a barometric pressure sensor (<http://www.allsensors.com>).

^b ILM-1500-R (0.90 kg) for Manta Flux payload and ILM-500-R (0.28 kg) for ScanEagle Flux and Imaging payloads. All have been factory modified to increase the power to the limit of the class 1M safety rating. Lidar units have also been repackaged to reduce weight.

^c Kipp & Zonen CMP3 and CGR3 (18 s for 95% response; 0.27 kg each) for Manta payloads, and Hukseflux SR03 and IR02 (1 and 18 s for 95% response, respectively; 0.18 kg each after custom modifications) for ScanEagle payloads.

breaking (Melville and Matusov 2002; Kleiss and Melville 2011). The electronic shutter trigger is typically set to five frames per second, and is phase locked to the GPS 1-pulse-per-second output. Flying at 28 m s^{-1} at an altitude of 300 m, with a 9-mm lens, the field of view is approximately $210 \text{ m} \times 280 \text{ m}$ (along \times across track) with 97% frame overlap, which is necessary to observe wave breaker evolution and important for boresight calibration. The ScanEagle Imaging payload also includes a FLIR (Wilsonville, Oregon) A325 longwave infrared camera, with a microbolometer detector sensitive in the $7.5\text{--}13\text{-}\mu\text{m}$ range.

The ScanEagles include nose-mounted, forward-looking cameras (Advance Security, Belleville, Illinois) for emergency navigation. The cameras also enable operators to identify phenomena of interest (e.g., frontal processes, enhanced breaking) and redirect the flight track during a mission. These cameras use a separate 2.4-GHz communication link.

The Radiometric payloads also include four radiometers for measuring shortwave and longwave up- and downwelling radiation. For the Manta, there is one upward-facing and one downward-facing Kipp & Zonen (Delft, Netherlands) CGR3 pyrgeometer, sensitive in the $4.5\text{--}42\text{-}\mu\text{m}$ spectral range, and upward- and downward-facing Kipp & Zonen CMP3 pyranometers, sensitive in the 310–2800-nm range. For the ScanEagle, Hukseflux (Delft, Netherlands) IR02s ($4.5\text{--}50\text{-}\mu\text{m}$) and SR03s (305–2800 nm) are used. The SR03s (used in the ScanEagle) have the advantage of a 1-s response time, compared to the 18-s response time of the CMP3s (used in the Manta). Surface temperature T_s is determined from the longwave upwelling $Q_{\text{LW}\uparrow}$ and downwelling $Q_{\text{LW}\downarrow}$ fluxes:

$$T_s = \left[\frac{Q_{\text{LW}\uparrow} - (1 - \epsilon)Q_{\text{LW}\downarrow}}{\epsilon\sigma} \right]^{1/4}, \quad (2)$$

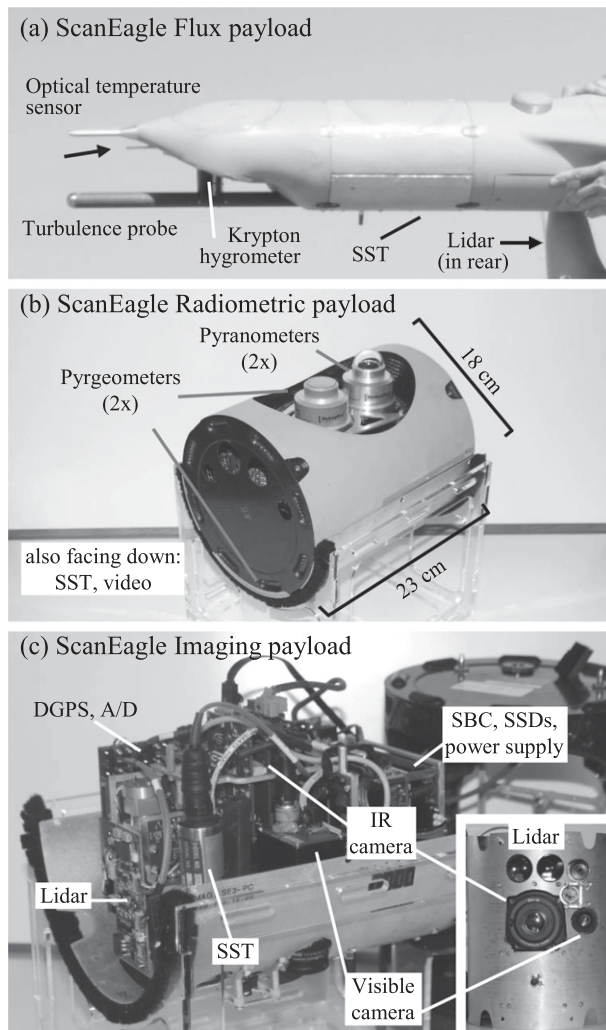


FIG. 3. Detailed photos of (a) the nose instrumentation for the ScanEagle Flux payload, (b) the ScanEagle Radiometric payload (top cover removed), and (c) the ScanEagle Imaging payload (removed from the fuselage section). Inset in bottom panel shows a bottom view of the Imaging payload.

where ϵ is the emissivity (≈ 0.98 for the sea surface) and σ is the Stefan–Boltzmann constant (Katsaros 1990). Dedicated radiometric SST sensors (custom Sea-Therms from Everest Interscience, Tucson, Arizona) are included in all three ScanEagle payloads, though they were not yet installed for the overwater flight tests.

The acquisition computer in the Manta payloads is a 1.6-GHz Intel Atom-based single-board computer (SBC) made by iEi Technology Corp. (Taipei, Taiwan), running Microsoft Windows XP. The ScanEagle payload acquisition computer is a Kontron (Munich, Germany) pITX-SP, a smaller SBC with similar capability, running Windows 7. At close range (< 300 m) before and after flight, we can remotely connect to these computers

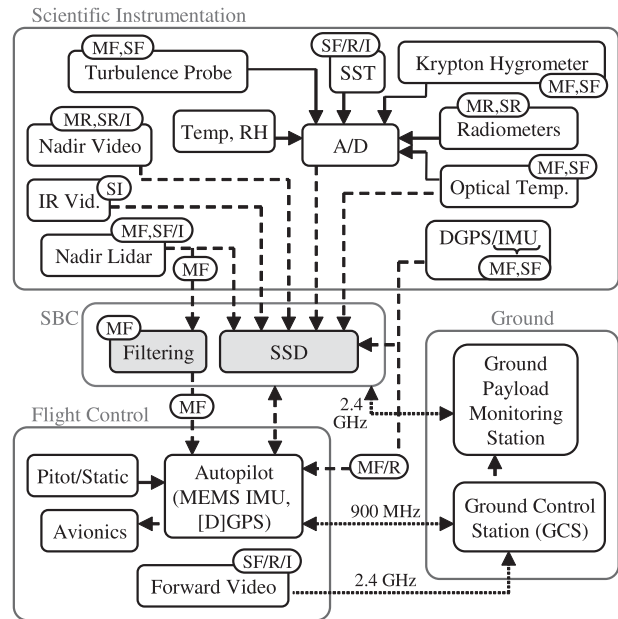


FIG. 4. Flowchart of instruments, acquisition hardware, and data flow for UAVs and payloads. Solid arrows represent analog data (measured with the analog-to-digital boards), dashed arrows represent digital communication, and dotted arrows represent radio communication. Unless noted with small lettering (see Table 3 for payload abbreviations), instruments and connections are common across all payloads. Initialization of instrumentation, filtering of lidar data, and logging of all data for each payload are performed with an SBC. Data are stored on onboard solid-state drives (SSDs). Additionally, 1-s averages of all analog signals, as well as a status update of onboard systems, are relayed through the 900-MHz flight control link to the ground control station, and passed through to the ground payload monitoring station. Direct 2.4-GHz “Wi-Fi” link to the ground payload monitoring station is for pre- and postflight communication and data transfer.

and transfer data via a 2.4-GHz Wi-Fi link. A National Instruments (Austin, Texas) USB-6211 16-bit, 16-channel module is used for analog data acquisition and synchronization control for the Manta payloads, and a USB-6218 (16 bits, 32 channels) for the ScanEagle. Analog signals are sampled at up to 200 Hz, and are phase locked to the GPS 1-pulse-per-second output. The 200-Hz sampling prevents aliasing and permits low-pass filtering of high-frequency noise sometimes observed in the pressure measurements (see section 4c). Communication of payload operational status and 1-s averages of all analog data through the 900-MHz radio link keeps the ground operators informed of atmospheric conditions and sensor status. All synchronization and logging of digital and analog data, as well as the IR imagery, are performed with a suite of acquisition software developed in National Instruments’ LabView. Visible video is acquired with IO Industries’ Streams 5 video software.

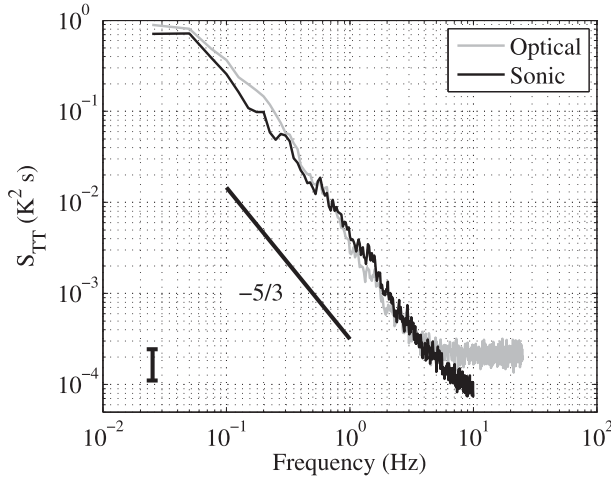


FIG. 5. Stationary outdoor comparison of temperature spectra from optical temperature sensor (Opsens OEM-MNT) and sonic anemometer (Campbell Scientific CSAT3). Vertical bar indicates the 95% confidence interval, calculated as described by Young (1995). A slope of $-5/3$ is predicted in the inertial subrange. A 17-min record is used, with 40-s Hanning windows used in the spectral calculation.

b. Turbulence probe design

A nine-port turbulence probe is mounted on the nose of the Manta and ScanEagle UAVs with the Flux payloads. The probe shaft is made from smooth 25.4-mm-diameter carbon fiber tubing, and is rigidly connected to the nose with a flush-mounted aluminum flange for the Manta, and a rigid aluminum and carbon mount for the ScanEagle. At the tip, a 25.4-mm stainless steel hemisphere has a center port and eight additional ports at 45° off axis, spaced evenly azimuthally (see Fig. 6). All pressure ports are 0.8 mm in diameter, small enough to discourage flow distortion around the probe. For the ScanEagle, we transitioned to a titanium hemisphere, and widened the main five pressure ports to 1.6 mm (ports 0, 1, 3, 5, and 7 in Fig. 6).

The 20.7-cm (8.2 probe diameters in length) carbon fiber tube houses the pressure transducers, and has eight static ports located 12.7 cm (5 probe diameters) from the tip, spaced equally azimuthally around the tube. The volume of air inside the static ports is internally sealed by O-rings and an aluminum annular piece, which reduces the static pressure measurement dependence on relative wind direction. Pneumatic tubing of 1.6-mm ($1/16$ in.) inner diameter, with lengths between 5.5 and 7.5 cm, connects the ports to the pressure sensors.

Pressure sensors, from All Sensors Inc. (Morgan Hill, California), measure the pressure differentials between four opposing off-axis port pairs, the pressure differential between the center nose and static ports, and also the absolute atmospheric pressure. The differential sensors

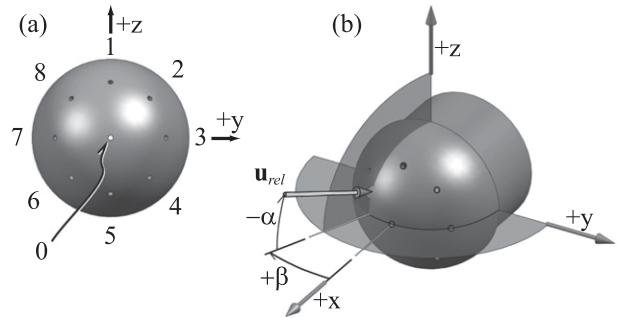


FIG. 6. Computer graphic of stainless steel (Manta) or titanium (ScanEagle) nine-port turbulence probe tip. (a) Front view, showing positions and nomenclature of the pressure ports. Differential pressure is measured between opposing port pairs ($\Delta P_\alpha = P_1 - P_5$, etc.) and between the center port and static ports located five probe diameters from the probe tip. Relative wind vector is calculated using Eqs. (3)–(7). (b) Perspective view, with definitions of the aircraft reference frame as well as α and β in terms of \mathbf{u}_{rel} , which in this drawing is directed in the $-x$, $+y$, and $-z$ direction. Note this is a nonstandard aircraft frame definition: it keeps $+z$ roughly aligned with the local Earth $+z$.

are temperature compensated and have an output of 0.5–4.5 V for a range of ± 2500 Pa, and a stated typical accuracy of 0.05% of the full range.

c. Georeferenced wind calculation

The turbulence probe measures relative wind velocity in three dimensions using an array of pressure ports on its hemispherical nose and differential pressure sensors. Refer to Fig. 6 for pressure port nomenclature and angle definitions. Following Kalogiros and Wang (2002), who demonstrated a five-port turbulence probe on the radome of a Twin Otter, we solve for angle of attack α , sideslip β , and dynamic pressure P_d assuming potential flow around a sphere:

$$\alpha = -\frac{1}{2} \arcsin \left(\frac{4}{9} \frac{\Delta P_\alpha}{P_d \cos \beta \sin 2\xi} \right), \quad (3)$$

$$\beta = -\frac{1}{2} \arcsin \left(\frac{4}{9} \frac{\Delta P_\beta}{P_d \cos^2 \alpha \sin 2\xi} \right), \quad \text{and} \quad (4)$$

$$P_d = \frac{4(P_0 - P_s)}{9 \cos^2 \alpha \cos^2 \beta - 5}, \quad (5)$$

where $\Delta P_\alpha = P_1 - P_5$ (=the pressure difference between the top and bottom nose ports), $\Delta P_\beta = P_3 - P_7$ (=pressure difference between right and left nose ports), and $P_0 - P_s$ is the measured pressure difference between the center port and the static ports. The constant ξ is the angular position of the ports relative to the along-probe axis, in this case 45° to maximize sensitivity of the pressure differential. Dynamic pressure P_d is the

TABLE 4. Sources of vertical wind uncertainty from a Monte Carlo simulation with $N = 10^6$ runs. See section 2d for details. Analysis assumes an airspeed of 28 m s^{-1} .

Platform	Manta	ScanEagle
Instrument uncertainties		
Pressure sensor uncertainty (Pa)	1.25	1.25
Attitude uncertainty (roll/pitch/heading) ($^\circ$)	0.007/0.007/0.011	0.005/0.005/0.008
DGPS/IMU velocity uncertainty (horizontal/vertical) (cm s^{-1})	2.00/1.00	2.00/1.00
Source of vertical wind uncertainty		
Pressure sensor uncertainty (cm s^{-1})	1.80	1.80
Attitude uncertainty (cm s^{-1})	0.34	0.24
DGPS/IMU velocity uncertainty (cm s^{-1})	1.00	1.00
Estimated vertical wind uncertainty (cm s^{-1})	2.09	2.07

difference between the pressure at the actual stagnation point and the static pressure. We initialize the unknowns as $\alpha = 0$, $\beta = 0$, and $P_d = P_0 - P_s$, and then Eqs. (3)–(5) are solved repeatedly and sequentially until α converges to within 0.001° . The asymmetry in Eqs. (3) and (4) is a result of the polar coordinate system (see Fig. 6).

We then use P_d to calculate the relative free stream airspeed, U_{rel} , using the Bernoulli equation along the streamline from $x = +\infty$ to the stagnation point:

$$U_{\text{rel}} = (2P_d/\rho)^{1/2}, \quad (6)$$

where ρ is the measured density of air and gravitational terms are neglected. Incorporating the attack and sideslip angles, the relative incident wind vector at the probe tip (\mathbf{u}_{rel} ; $U_{\text{rel}} = |\mathbf{u}_{\text{rel}}|$) is calculated as follows (Kalogiros and Wang 2002):

$$\mathbf{u}_{\text{rel}} = \begin{bmatrix} u_{\text{rel}} \\ v_{\text{rel}} \\ w_{\text{rel}} \end{bmatrix} = \begin{bmatrix} -U_{\text{rel}} \cos \alpha \cos \beta \\ U_{\text{rel}} \cos \alpha \sin \beta \\ U_{\text{rel}} \sin \alpha \end{bmatrix}. \quad (7)$$

Refer to Fig. 6 for the nonstandard reference frame definition [$+x$ points out the aircraft nose, $+y$ points out the left (port) wing, and $+z$ points out the top of the aircraft]. Similar expressions for u_{rel} , v_{rel} , and w_{rel} can be constructed using pressure differences between the diagonal nose ports ($P_2 - P_6$; $P_4 - P_8$), and then rotating the result 45° about the x axis.

The absolute wind vector in an Earth reference frame is then determined by rotating the relative wind from aircraft coordinates into an Earth reference frame and adding that to the velocity of the UAV over ground, determined with the DGPS/IMU, and including the lever arm motion:

$$\mathbf{u} = \mathbf{u}_{\text{uav}} + \mathbf{R}(\mathbf{u}_{\text{rel}} + \boldsymbol{\omega} \times \mathbf{r}), \quad (8)$$

where \mathbf{u}_{uav} is the velocity of the IMU in an Earth reference frame; \mathbf{R} is the rotation matrix generated from

sequential roll, pitch, and yaw rotations; $\boldsymbol{\omega}$ is the rotational velocity of the aircraft in aircraft coordinates; and \mathbf{r} is the position vector from the IMU to the turbulence probe sensing tip, in aircraft coordinates. The expanded component-wise version of Eq. (8) is often found in the literature (e.g., Lenschow 1986).

d. Uncertainty analysis

To estimate georeferenced wind measurement uncertainty, we perform a Monte Carlo simulation of the wind georeferencing algorithm with the number of samples $N = 10^6$. Pressure differentials and DGPS/IMU-derived velocity and attitude [the input variables to Eqs. (3)–(8)] are sampled from Gaussian distributions with means corresponding to constant altitude straight-line flight and one standard deviation (1σ) widths given by individual component typical accuracy specifications from the manufacturer. Errors in the input variables are considered uncorrelated. After running each set of $N = 10^6$ samples through the georeferencing equations, uncertainty is estimated as the standard deviation of the distribution of final georeferenced wind components. Input parameter accuracies and final uncertainties of vertical wind are summarized in Table 4.

By this method, we estimate georeferenced wind 1σ uncertainties as $\pm 4.5 \text{ cm s}^{-1}$ for horizontal and $\pm 2.1 \text{ cm s}^{-1}$ for vertical; these are comparable to the accuracies estimated using reverse-heading maneuvers discussed in section 4b. Uncertainties calculated using this method agree very well (within 1%) with uncertainties calculated by propagating instrument errors through linearized wind georeferencing equations, as described by Enriquez and Friehe (1995). For the vertical wind measured by the ScanEagle Flux payload, 59% of the variance is due to errors in the pressure measurements, 33% to errors in the DGPS/IMU vertical velocity measurement, and 8% to errors in the attitude measurement. There is negligible uncertainty due to errors in the lever arm velocity measurement [$\boldsymbol{\omega} \times \mathbf{r}$ in Eq. (8)].

3. Turbulence probe calibration and validation

a. Wind tunnel calibration

To compensate for turbulence probe and sensor imperfections and distortion of the flow by the aircraft, empirical corrections to the potential flow solution are formulated using measurements from wind tunnel experiments, similar to the wind tunnel calibrations performed by Garman et al. (2006) for a BAT probe. The ScanEagle nose and the Manta nose and fuselage, with turbulence probes and Flux payloads, were each placed in San Diego State University's low-speed wind tunnel (<http://aerospace.sdsu.edu/research.html>). The tunnel has servo motor control of attack and sideslip angle, and attitude was also measured by the payload's IMU and acquisition system. An external pitot-static tube was positioned above the turbulence probe (in the same vertical plane), fixed 18 cm below the top of the tunnel wall, with a factory-calibrated Druck pressure transducer (Druck Limited, Leicester, United Kingdom) to measure the reference dynamic pressure. Pressure, temperature, and attitude measurements were recorded by the UAV's onboard acquisition system.

Tests were repeated at nominal wind speeds of 20, 25, 30, 35, and 40 m s^{-1} for the Manta; and 20, 24, 28, 32, and 36 m s^{-1} for the ScanEagle, covering aircraft stall to dash speeds (mission speeds are typically 25–33 m s^{-1} for both UAVs). For the Manta, holding the sideslip angle constant at 0° , the angle of attack was varied from -9° to $+11^\circ$ at 1° increments, with nominally 60 s of 200-Hz data recorded at each angle. Holding the angle of attack constant at 0° , the sideslip angle was varied from -9° to $+9^\circ$ at 1° increments for wind speeds of 20 and 25 m s^{-1} , and from -8° to $+8^\circ$ at 2° increments for 30, 35, and 40 m s^{-1} . Similarly, for the ScanEagle, attack and sideslip angles were varied independently from -10° to $+10^\circ$ at 1° increments for all wind speeds. These ranges encompass the limits of incident flow angles observed during flight.

Second-order polynomial functions of probe-measured dynamic pressure and attack angle are least squares fit to the reference dynamic pressure measured by the external Druck transducer. The resulting calibrated dynamic pressure is then used to recalculate the attack and sideslip angles [Eqs. (3)–(5)]. Third-order polynomial functions of the recalculated angles are then fit to their prescribed values. As in Garman et al. (2006), sideslip and attack angles are treated independently. These calibrations are subsequently applied to all testing and in-flight turbulence probe relative wind measurements.

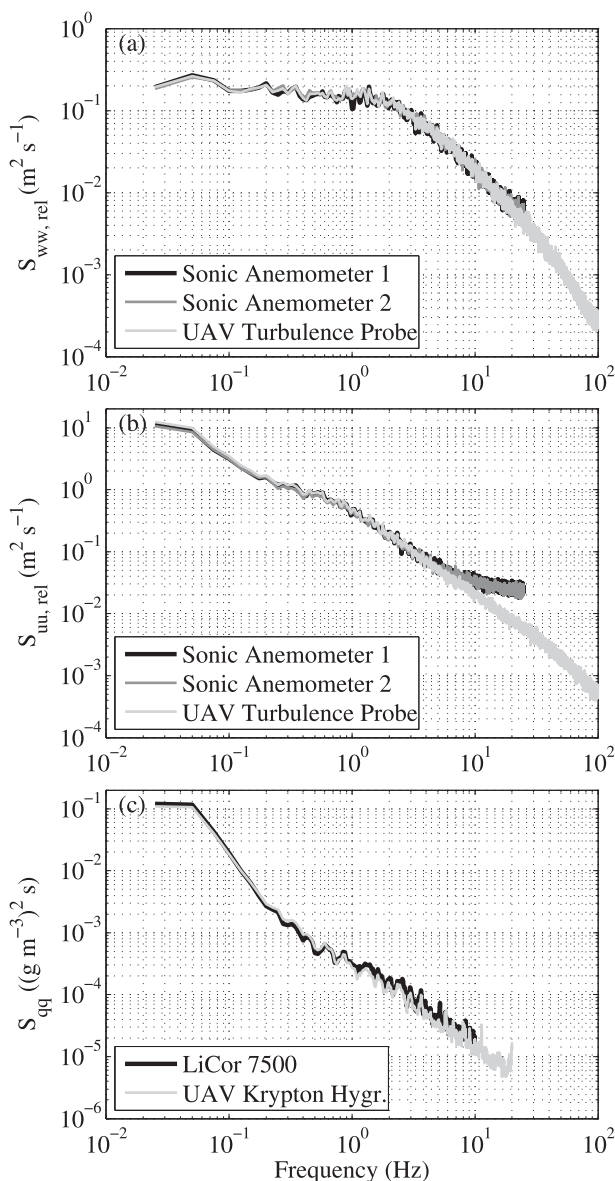


FIG. 7. Spectra of (a) vertical and (b) horizontal relative wind components, calculated with the sonic anemometer and turbulence probe relative wind data from a ground-vehicle-based test of the Manta UAV Flux payload. Note the superior frequency response of the turbulence probe when compared with the sonic anemometers. (c) Water vapor spectra comparison of the krypton hygrometer and the LI-7500. A 30-min record is considered, with 40-s Hanning windows used in the spectral calculation.

b. Ground-vehicle-based turbulence probe validation

Experiments with the Manta fuselage and Flux payload mounted on a pickup truck were conducted in March and November 2010 (see Fig. 1d). These experiments were performed in order to verify the design of the turbulence probe, using the final sensors and

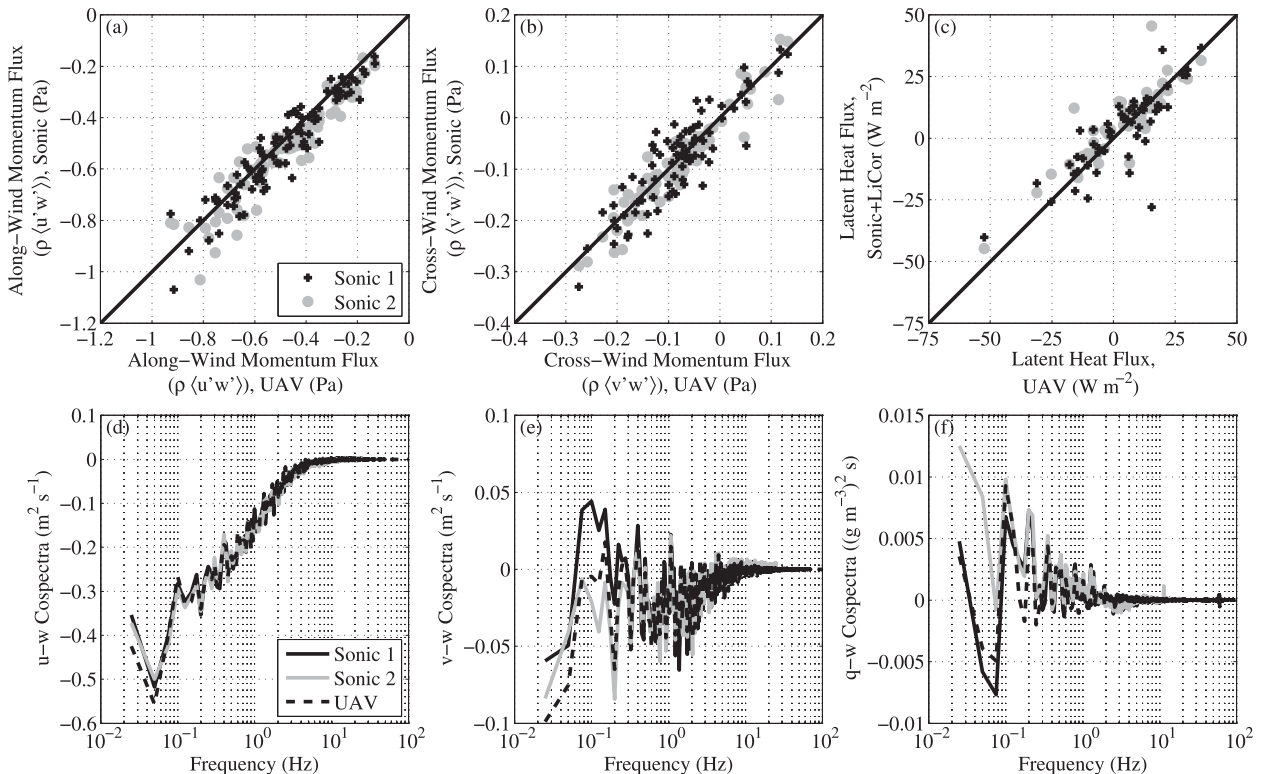


FIG. 8. Comparison of momentum and latent heat flux, and corresponding cospectra, measured by the Manta Flux payload with those measured by CSAT3 sonic anemometers and the LI-7500 hygrometer during ground-vehicle-based tests. Shown in black in (a)–(c) are 1:1 lines. Cospectra and fluxes are calculated in a moving reference frame, fixed with respect to the respective probes. Relative wind speed was $23 \pm 1 \text{ m s}^{-1}$ (1σ). Fluxes are calculated from integrated cospectra over 40-s segments, with 30 min of data total. See sections 3b and 4c for details of the flux calculations.

acquisition methods, and also to test the complete Flux payload in a flight-like scenario. An aluminum pipe structure was rigidly connected to a pickup truck's full-length roof rack, holding the turbulence probe 1.2 m above the cab, and the truck [General Motors Company (GMC) Sierra SLT] was driven at freeway speeds (around 26 m s^{-1}). Two research-grade CSAT3 sonic anemometers (Campbell Scientific) were mounted on the structure with their axes carefully aligned parallel to the turbulence probe axis and with sampling volumes spaced 27 cm laterally (one on either side) and 5 cm ahead of the turbulence probe tip. An LI-7500 open-path gas analyzer (LI-COR, Lincoln, Nebraska) was also installed for comparison with the UAV krypton hygrometer.

The calibrations determined from wind tunnel tests are applied to the turbulence probe measurements, as is the additional scaling determined from reverse flight maneuvers, which will be described in section 4a. The instantaneous velocity vectors for each instrument are rotated in order to zero the mean vertical and crosswind components of the 30-min sample segment discussed here, which aligns the x coordinate of the reference

frame of each sensor along a mean streamline. After averaging into 30-s bins, root-mean-squared differences between wind speed measurements of the turbulence probe and the two sonic anemometers are 2.7 and 2.0 cm s^{-1} for vertical, and 2.4 and 2.9 cm s^{-1} for crosswind, which are within the stated accuracies of the CSAT3 ($\pm 4 \text{ cm s}^{-1}$ offset error $\pm 2\%$ of the reading for vertical, and $\pm 8 \text{ cm s}^{-1}$ offset error and $\pm 2\%$ of the reading for horizontal; <http://www.campbellsci.com/csats3>). Comparisons of relative horizontal wind, relative vertical wind, and water vapor spectra are presented in Fig. 7, showing strong agreement between the UAV-derived measurements and the sonic anemometers and LI-7500 measurements. As seen in Fig. 7, the sonic anemometer horizontal wind reaches its noise floor at frequencies in which turbulence probe measurements are still reliable.

Fluxes normal to the mean streamline and in a vertical plane are calculated using integrated cospectra of relative vertical wind w with relative horizontal wind components u and v for vertical flux of horizontal momentum, and with water vapor density q for latent heat flux—the methods for which are described in detail in section 4c.

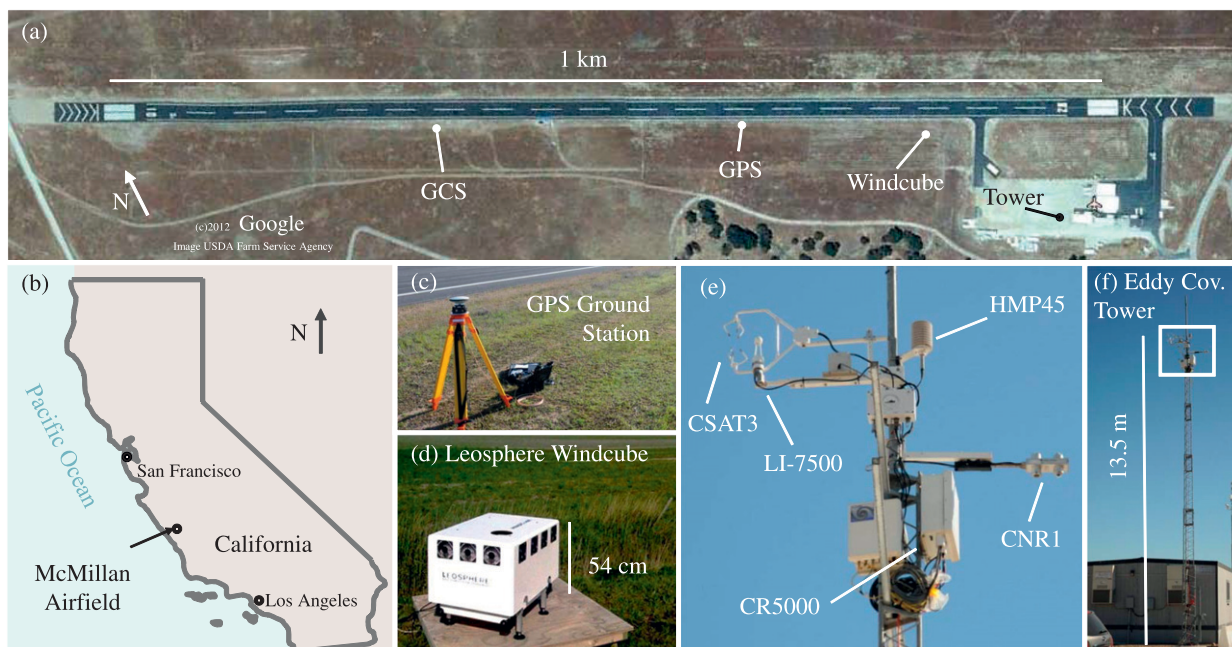


FIG. 9. (a) McMillan Airfield runway, (b) location, and (c)–(f) ground instrumentation used during Manta UAV flight tests on 24–28 Jan 2011. Location of the GCS is shown in (a) and photographs of the (c) GPS ground station, (d) Leosphere Windcube, and (f) eddy covariance tower. Note the contrast between the black paved runway and the lighter gravel and vegetation near the tower.

Comparisons between the fluxes and cospectra measured by the turbulence probe and those measured by the sonic anemometers are shown in Fig. 8. Segments used are 40 s in length, and a 5-Hz low-pass cutoff is applied to the integration of cospectra, corresponding to the noise rolloff frequency seen in the spectra of the sonic anemometer horizontal wind in Fig. 7b. The length of the record is approximately 30 min, during which time the truck traveled approximately 48 km through varied local terrain. Because of the inhomogeneity of the environment sampled, there is nonzero cospectral energy at lower frequencies. These direct flux comparisons, however, are still informative as they compare covariance over the same frequency range.

After averaging the 40-s fluxes into 10-min bins, RMS differences between the turbulence probe and the two sonic anemometer fluxes are 0.023 and 0.047 Pa ($1 \text{ Pa} = 1 \text{ N m}^{-2}$) for the along-wind component of vertical momentum flux, 0.013 and 0.010 Pa for crosswind vertical momentum flux, and 1.1 and 3.7 W m^{-2} for latent heat flux. RMS differences between the turbulence probe and sonic anemometer fluxes are comparable to or less than the RMS differences between those calculated by the two sonic anemometers, though it is unclear how much of this is because of the larger physical separation between the two sonic anemometers (54 cm) than between the turbulence probe and each sonic anemometer (27 cm).

4. Engineering flight tests over land

Engineering flight tests of the Manta Flux and Radiometric payloads were performed 24–28 January 2011 over land at McMillan Airfield in Camp Roberts, California (35.7190°N , 120.7703°W). Local terrain (within 5 km of the airfield) includes hills up to 250 m above the runway elevation. A tower-mounted eddy covariance system was installed for comparison of some of the atmospheric measurements. The sensors were positioned at 13.5 m AGL on the tower, which was located 100 m south of the east end of the runway. A Leosphere (Orsay, France) WindCube, which measures vertical profiles of 3D wind, was also deployed during the experiment, but the very clear atmospheric conditions did not provide enough return signal for laser Doppler measurements. See Fig. 9 for locations of instruments relative to the runway.

The experiment was dominated by mainly clear sky, and light and variable surface winds, which, as measured by the 13.5-m tower, never exceeded 3 m s^{-1} ; however, as we explain in section 4d, an 8 m s^{-1} atmospheric jet was observed by the Manta Flux payload during one flight at about 1 km AGL. As measured by the tower, air temperature ranged from a 1° – 3°C minimum in the mornings to a 21° – 23°C maximum in the afternoons; relative humidity ranged from around an 80% maximum in the mornings to a minimum of around 17% in the afternoons.

Flight paths were selected for laser altimeter testing, turbulence probe calibration and validation (repeated reverse-heading tracks), and vertical atmospheric profiling. The Manta with the Flux payload flew racetrack patterns with low-level segments down to 23 m AGL, using laser altimetry for terrain following. The two Mantas performed vertically stacked flights, including the first known demonstration where the lower Manta's altitude was maintained by filtered laser altimeter measurements during stacked flight, flying as low as 30 m AGL. During straight-and-level segments of stacked flight, the horizontal distance between the two Mantas was consistently within 1 m in cross track, and within 20 m (<1 s) in along-track directions. This section details the in-flight turbulence probe calibration refinement methods, flux calculations, observations of atmospheric boundary layer structure, and comparisons with the eddy covariance tower.

a. In-flight turbulence probe calibration refinement

Many studies have proposed various methods for in-flight probe calibration (e.g., Khelif et al. 1999; Esposito 2008), but few (e.g., Garman et al. 2006) combine wind tunnel calibrations with in-flight calibrations to improve the quality of the final wind measurements.

To account for yaw mounting offset between the IMU and the turbulence probe, we introduce a to-be-determined sideslip angle offset $C_{0,\beta}$ (IMU measurements of pitch and roll are known absolutely for the wind tunnel measurements, so offsets in pitch and roll are already taken into account with the initial tunnel calibration). To account for the difference in dynamic pressure from the tunnel-calibrated solution to the actual free stream dynamic pressure, we also introduce a linear scaling factor to the calculated dynamic pressure $C_{1,Pd}$. We explore the effect that varying these terms has on georeferenced wind using measurements from overlapping reverse-heading maneuvers conducted at various altitudes, airspeeds, and wind speeds. The overlapping regions ranged from 1.5 to 3 km, and the time between the start of one pass and the finish of the corresponding reverse pass was typically less than 4 min. Wind measurements from sequential passes are each binned into 500-m segments, and we determine values for $C_{0,\beta}$ and $C_{1,Pd}$, which minimize the squares of the differences in horizontal georeferenced component wind between the two sequential passes:

$$\text{cost} = \frac{1}{B} \sum_{b=1}^B [(\langle u \rangle_{b,2} - \langle u \rangle_{b,1})^2 + (\langle v \rangle_{b,2} - \langle v \rangle_{b,1})^2], \quad (9)$$

where $\langle u \rangle_{b,p}$ and $\langle v \rangle_{b,p}$ are Earth-referenced north and east component winds averaged into bin $b = 1, \dots, B$ and pass $p = 1, 2$.

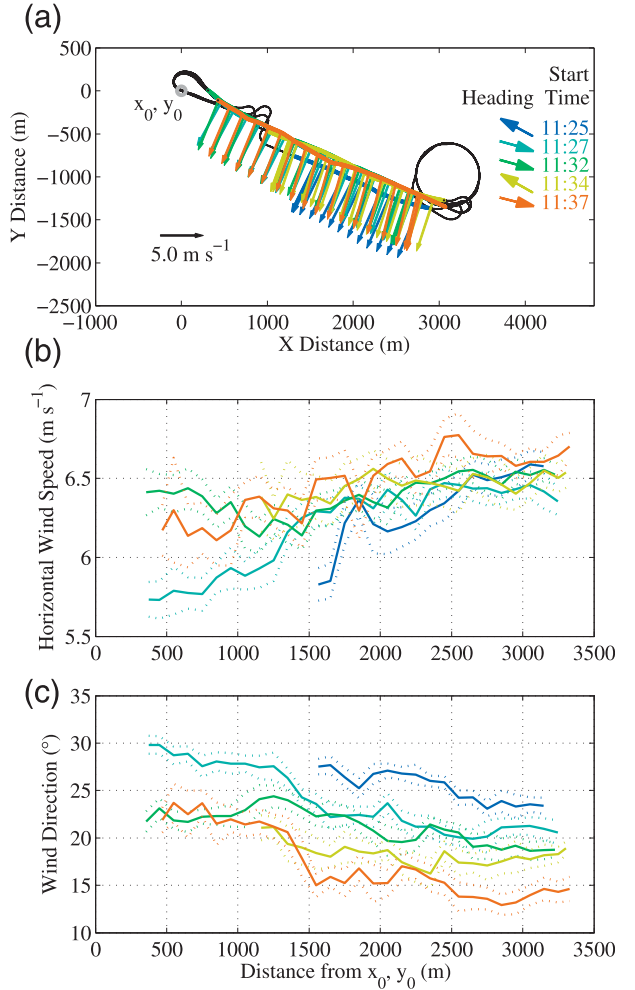


FIG. 10. (a) Sample repeated reverse heading flight paths (1280 ± 1 m AGL) from Manta UAV flights at McMillan Airfield on 27 Jan 2011, with measured horizontal wind vectors (pointing with the wind) at 5-s intervals; mean heading vectors and start times (LT = UTC - 8 h) for each pass are given. Wind (b) speed and (c) direction in 100-m bins are shown. Dotted lines indicate $\pm 1\sigma$ within bins. Note the wind turns more than 10° over the course of 20 min, and changes by up to 10° from one end of a pass to the other. Not included is one westbound pass (1129 LT start), during which the UAV changed course during a temporary communication time out. With the Manta's 900-MHz antenna on the top of the fuselage, line-of-sight communication was suboptimal when the UAV was directly above the ground station.

First, we use a “brute force” method to explore a large parameter space of $C_{0,\beta}$ and $C_{1,Pd}$, to ensure that the final result will be at the global cost minimum. The optimal $C_{0,\beta}$ and $C_{1,Pd}$ determined from this brute force method are then provided as initial estimates for a nonlinear optimization routine that uses the Nelder–Mead simplex algorithm, implemented with the *fminsearch* routine in MathWorks' MATLAB (see, e.g., Lagarias et al. 1998). We calculate optimal $C_{0,\beta}$ and $C_{1,Pd}$ for each of 17 reverse-heading

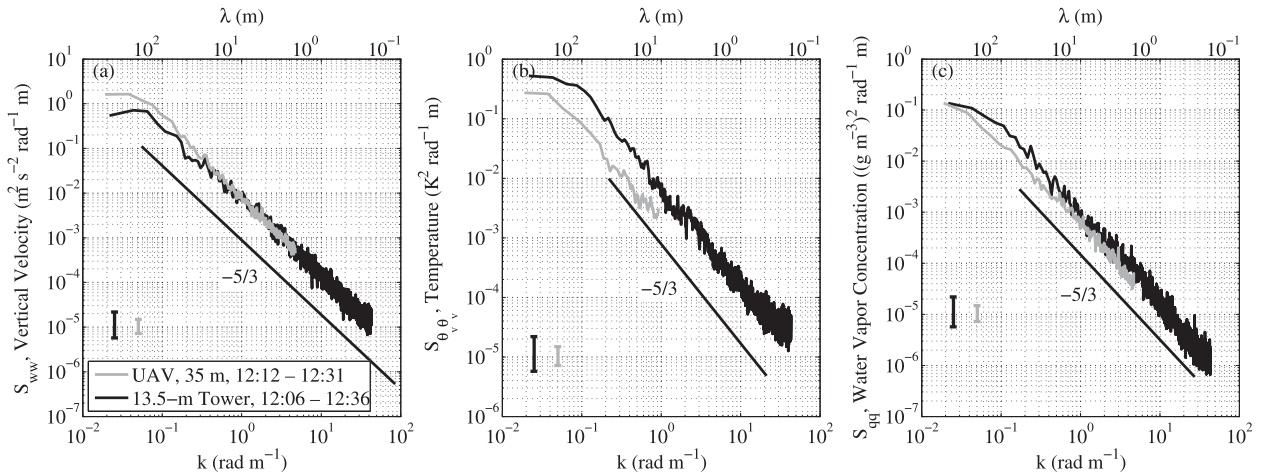


FIG. 11. Spectra of (a) vertical wind velocity, (b) virtual potential temperature, and (c) water vapor density as measured by the fixed 13.5-m eddy covariance tower and the instrumented Manta UAV flying adjacent to the tower at 35 m AGL, on 28 Jan 2011. We assume Taylor's hypothesis to transform spectra into the wavenumber domain (see text). For the Manta, 310 s of data are considered, with 10-s Hanning windows used in the spectral calculation. For the tower, 30 min of coincident eddy flux data are used, with 200-s windows. Time ranges (LT = UTC – 8 h) are given; vertical bars indicate 95% confidence intervals. We attribute the spectral offsets in temperature and water vapor to variability within the surface layer likely resulting from the surrounding man-made structures and inhomogeneous surfaces (see Fig. 9).

pass pairs, and taking the mean, we obtain $C_{0,\beta} = -1.50^\circ (\pm 0.15^\circ, 1\sigma)$ and $C_{1,\text{Pd}} = 1.043 (\pm 0.005)$, with $\langle \text{cost} \rangle = 0.029 \text{ m}^2 \text{ s}^{-2}$. We use the mean values of $C_{0,\beta}$ and $C_{1,\text{Pd}}$ for all subsequent georeferenced wind calculations.

b. Absolute georeferenced wind accuracy estimation

To make an estimate of georeferenced wind accuracy, we examine the same 17 reverse-heading pass pairs after final georeferencing, with winds from each pass horizontally binned to 500 m. An example of horizontal wind speed and direction measured during several repeated reverse-heading maneuvers is shown in Fig. 10. We estimate georeferenced wind measurement accuracies as half of the RMS difference between collocated binned velocity components from sequential passes: $\pm 9.8 \text{ cm s}^{-1}$ in the horizontal wind and $\pm 4.3 \text{ cm s}^{-1}$ in the vertical. These values include the changing physical conditions in the short time between subsequent passes (Fig. 10), and we consider them consistent with the smaller theoretical uncertainties calculated in section 2d.

c. Spectra and flux calculations

A comparison of spectra of vertical wind from the eddy covariance tower and a series of low-level (30 m AGL) UAV passes is shown in Fig. 11, along with spectra of atmospheric temperature and water vapor density. We assume Taylor's hypothesis to transform spectra into the wavenumber domain using, for the UAV, the mean airspeed during the passes (33.2 m s^{-1}), and for the eddy covariance tower, the mean horizontal wind speed (1.5 m s^{-1}). The spectra illustrate that the

UAV is capturing the inertial subrange of the turbulent flow (energy density $\propto k^{-5/3}$, where wavenumber $k = 2\pi/\lambda$ and λ is wavelength). The inertial subrange of turbulence is observed down to wavelengths of approximately 1.3 m (25 Hz) for the vertical wind and humidity, and to 6.6 m (5 Hz) for temperature. The sample temperature spectrum from the UAV has about 2.5–3 times less energy than the spectrum measured with the eddy covariance tower, and the vapor spectrum about 1.5 times less, which we attribute to the large vertical and horizontal inhomogeneity of temperature and humidity variation in the surface layer, as observed in low-level profiles. The stark contrast between the asphalt runway and the light gravel near the tower is notable in Fig. 9 and is likely to affect the surface layer dynamics. Based on the good agreement of sensors in direct comparisons (Figs. 5 and 7c), we consider the UAV temperature and water vapor measurements valid.

Using the eddy covariance method, fluxes are calculated using covariances of vertical wind w with horizontal wind components u and v for vertical flux of horizontal momentum in along- and crosswind directions (τ_x and τ_y , respectively), with virtual potential temperature θ_v for sensible heat flux Q_S , and with water vapor density q for latent heat flux Q_L :

$$\tau_x = \rho \langle u'w' \rangle, \quad (10)$$

$$\tau_y = \rho \langle v'w' \rangle, \quad (11)$$

$$Q_S = \rho C_p \langle \theta_v'w' \rangle, \quad \text{and} \quad (12)$$

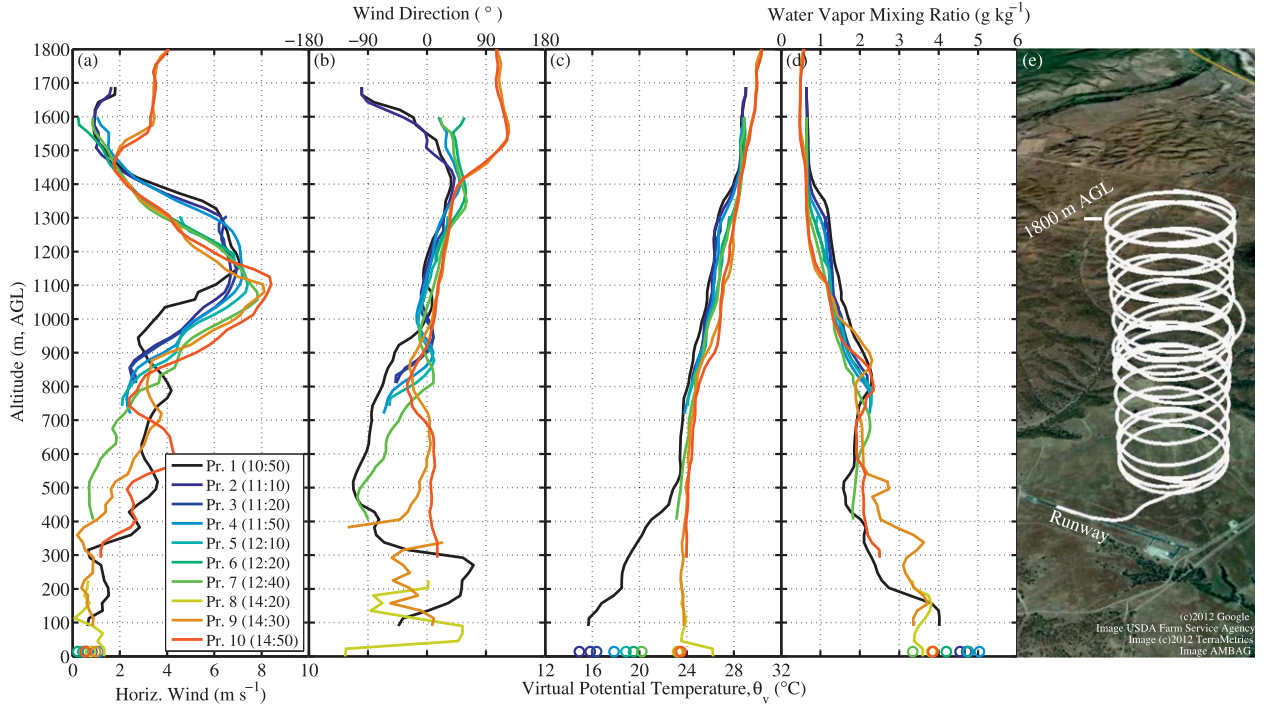


FIG. 12. Vertical profiles of atmospheric measurements from Manta UAV engineering flight tests on 27 Jan 2011 at McMillan Airfield. Each color represents one helical vertical sounding, with local start times (LT = UTC - 8 h) given. Data are averaged into 45-m vertical bins with 50% overlap. Round circles at the base of each panel represent 13.5-m tower measurements, averaged over the time of the corresponding profile. Horizontal wind (a) magnitude and (b) direction measured with the turbulence probe. (c) Virtual potential temperature and (d) water vapor mixing ratio measured by the HMP45C humidity/temperature sensor. Local maxima in the vapor concentration below 600 m in the afternoon profiles are also evident in the krypton hygrometer data. (e) Perspective view of a sample helical ascent and descent. Orbit diameter is approximately 750 m.

$$Q_L = L_v \langle q'w' \rangle, \quad (13)$$

where C_p is the specific heat of air, L_v is the latent heat of vaporization of water, angle brackets indicate ensemble averages (assumed equivalent to time averages), and primes indicate turbulent quantities (i.e., $u' \equiv u - \langle u \rangle$). Covariance terms are calculated using integrated cospectra so that the behavior and quality of the covariance calculation can be investigated in frequency space (see, e.g., Friehe et al. 1991; Beardsley et al. 1997; Khelif et al. 1999; French et al. 2007). Examining the power spectra of relative wind components, we see a small peak around 28 Hz, coincident with a peak seen in the spectra of vertical velocity as measured by the IMU. This peak was not visible either in stationary engine tests or ground-vehicle-based tests, suggesting it is related to propeller- and flight-induced dynamics and vibration. It is not at a frequency expected by direct propeller influence [for three propeller blades: $5000 \text{ rpm} \times 3 \times (1 \text{ min}/60 \text{ s}) = 250 \text{ Hz}$], though it could be attributable to aliasing of these high-frequency effects. Because we observe negligible cospectral energy contribution above 10 Hz, we limit the cospectra integration to frequencies below 10 Hz.

Following French et al. (2007), we impose quality checks for flux measurements by only using segments where integrated cospectra are largely monotonic and exhibit a well-defined energy-containing region. This method is described in more detail, with an accompanying figure, in section 5. We find the majority of covariant energy between 0.1 and 5 Hz, corresponding to wavelengths between 280 and 6 m (given the UAV's airspeed of 28 m s^{-1}). For most analysis, selected integration time was 45 s, corresponding to spatial scales of 1260 m.

d. Vertical profiling and observations of atmospheric structure

Multiple helical vertical soundings were conducted up to 1900 m AGL. Vertical profiles of wind speed and direction, virtual potential temperature (potential temperature of dry air at the same density), and water vapor mixing ratio are shown in Fig. 12. Data are from 10 helical soundings throughout the day of 27 January 2011. The prescribed ascent/descent rate was between 2 and 6 m s^{-1} (typically 2 m s^{-1}), with an orbit diameter of 750 m and orbit period of around 85 s. The local atmosphere is seen to be stable at all altitudes in all soundings

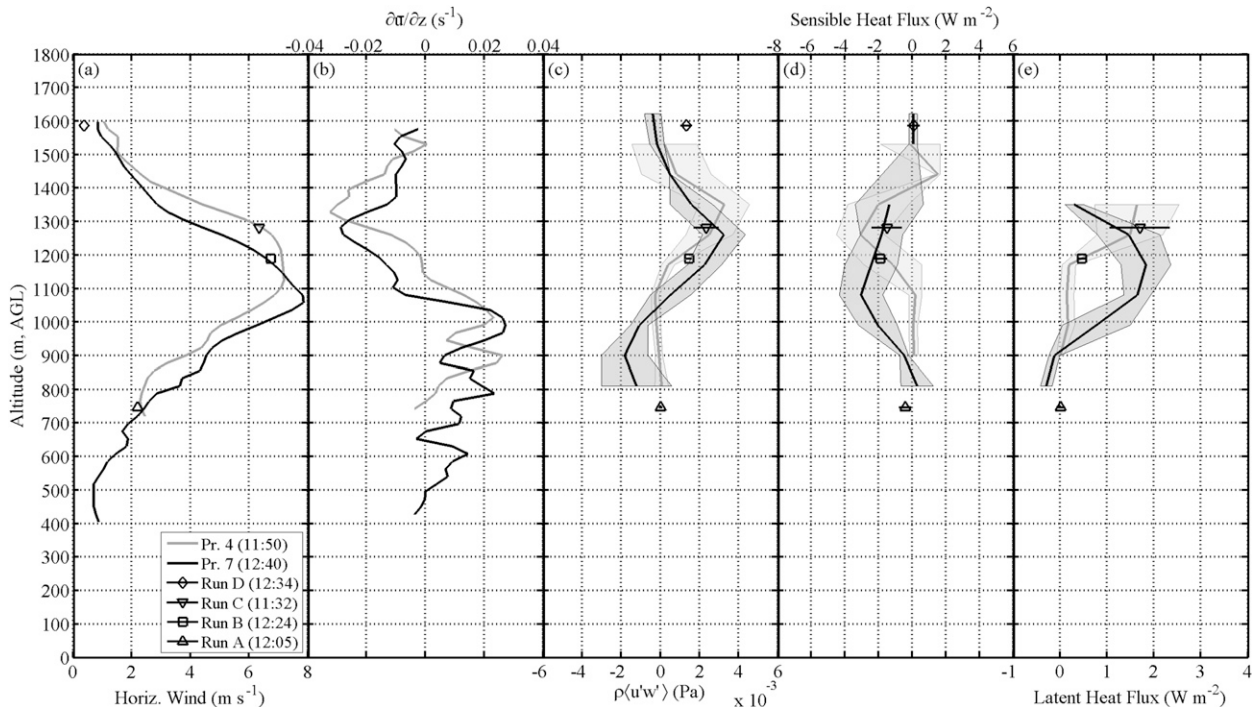


FIG. 13. Sample vertical profiles of turbulent fluxes from Manta UAV engineering flight tests on 27 Jan 2011 at McMillan Airfield. Shown are two sample profiles of (a) horizontal wind, (b) local vertical shear of horizontal wind, (c) vertical flux of horizontal momentum, (d) sensible heat flux, and (e) latent heat flux, measured within vertical helical profiles. Symbols correspond to measurements from straight-and-level passes, interspersed among the profiles in altitude and time (cf. Fig. 10a). Local start times (LT = UTC – 8 h) are given. Fluxes are calculated by integration of cospectra from 45-s segments and are averaged into 180-m vertical bins with 50% overlap. Flux calculations are quality controlled; rejected measurements are not included in the bin averaging. Bins must have at least two valid measurements to be shown. Error bars and shaded areas correspond to ± 1 standard error of individual flux calculations. Winds within each 45-s segment are rotated in order to zero the mean crosswind. Latent heat flux measurements above 1380 m AGL failed (see text).

(except in the first tens of meters above the asphalt runway in the late afternoon), with the gradient Richardson number $Ri_g \geq 1$, where

$$Ri_g = -\frac{g}{\bar{p}} \frac{\partial \bar{p}}{\partial z} \left(\frac{\partial \bar{u}}{\partial z} \right)^{-2}, \quad (14)$$

in which g is gravitational acceleration, \bar{p} is mean local density, and $\partial \bar{u} / \partial z$ is the local vertical shear of mean horizontal wind; overbars indicate vertically averaged quantities (in this case, 45-m bins are used, with 50% overlap). A logarithmic wind profile is not observed because of the light wind conditions, very stable structure, and inhomogeneous local terrain.

A wind jet of up to 8 m s^{-1} was observed, centered at 1200 m AGL in the morning (1050 LT), lowering to 1050 m AGL by the midafternoon (1450 LT) and rotating clockwise by about 27° . This jet does not share the characteristics of a classic low-level nocturnal jet (e.g., Banta et al. 2006; Blackadar 1957), and is therefore likely of ageostrophic origin. Smaller persistent features are also notable, such as the slight clockwise rotation of wind in

the high shear region just below the jet maximum. An increase in stratification (visible in the virtual potential temperature profile) is coincident with the shear region just above the jet peak (and likely capping the boundary layer), consistent with large-eddy simulations of similar features in previous studies (Taylor and Sarkar 2008).

Cospectra used in flux calculations were calculated over 45-s segments (half an orbit) along the helical flight paths, and binned into 180-m vertical bins with 50% overlap. Fluxes calculated from straight-and-level passes (using 45-s segments), interspersed in altitude and time, are largely in agreement, within ± 1 standard error. Following Vickers and Mahrt (1997), we find that, in the high shear region, approximately 5%–10% of the calculated momentum flux may be attributable to correlations of vertical wind fluctuations with aircraft altitude fluctuations, as the UAV moves through vertical gradients of horizontal wind. Samples of flux measurements within two vertical profiles are shown in Fig. 13. Fast-response water vapor measurements above around 1380 m AGL failed; the extremely dry environment was outside of the selected sensor range (the range was

subsequently extended). We observe consistent positive (upward) momentum flux in the negative shear region above the jet maximum, and negative momentum flux in the positive shear region below the jet maximum. Latent heat flux is seen to be close to zero or positive throughout, with a maximum in the high shear region above the jet maximum, coinciding with the sharpest gradient in water vapor. Sensible heat flux is mainly negative throughout, with a peak coinciding with a region of high $\partial\theta_v/\partial z$.

Following Turner (1973), neglecting small transport and diffusion terms, we can derive an equation for the time evolution of the turbulent kinetic energy E_k [$\equiv (1/2)(\langle u'^2 \rangle + \langle v'^2 \rangle + \langle w'^2 \rangle)$] for stratified, horizontally homogeneous turbulent flow:

$$\frac{dE_k}{dt} = -\langle u'w' \rangle \frac{\partial U}{\partial z} - \frac{g}{\bar{\rho}} \langle \rho'w' \rangle - \varepsilon, \quad (15)$$

where the first two terms on the right-hand side are turbulent production and work against buoyancy force, and ε is viscous dissipation. The covariance in the buoyancy flux, $\langle \rho'w' \rangle$ is calculated with integrated co-spectra, as previously discussed. Viscous dissipation is calculated by a least squares fit of $k^{-5/3}$ in the inertial subrange of the vertical wind power spectra S_{ww} with

$$S_{ww} = C\varepsilon^{2/3}k^{-5/3}, \quad (16)$$

where $C = 0.65$ (e.g., Pope 2000). Within the high shear region above the jet, we find a near-steady-state condition with production balanced by dissipation and buoyancy flux—that is, setting $dE_k/dt = 0$, the residual of the right-hand side of Eq. (15) is within the estimated standard error in turbulence measurements (the square root of the sum of squares of the standard errors of the individual terms). In other regions, the residual is outside the estimated standard error, implying that E_k is evolving in time or that there is vertical turbulent or pressure transport from internal waves, as is seen by Pham et al. (2010) in numerical simulations of a stable stratified jet, though this is difficult to quantify observationally with our measurements.

e. Lidar and imagery

Nadir-pointing lidar range data from the Manta Flux payload have been georeferenced as described in Reineman et al. (2009), with the position and attitude from the DGPS/IMU interpolated to the time of each lidar pulse. Figure 14 shows sample lidar data taken 28 January 2011 with 10 overlapping flights approximately parallel to the runway, offset from the runway by approximately 25 m as a safety precaution (operators were stationed on the southern edge

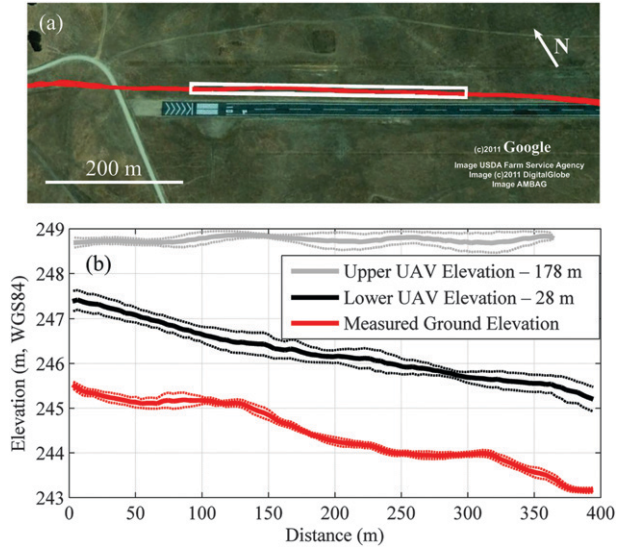


FIG. 14. (a) Repeat track lidar topography near the runway, with data overlaid on Google Earth imagery. Two Manta UAVs were in stacked formation: the top UAV was programmed to maintain a constant GPS altitude for these segments, while the bottom UAV was programmed to maintain constant height above ground using measurements from the lidar. Over this region, the bottom UAV maintained an altitude over ground of 29.8 ± 0.9 m. (b) Profile view of 10 passes of lidar data and the bottom UAV's altitude (offset by -28 m for clarity) and four passes of the top UAV's altitude (offset by -178 m). Data are from within the $400 \text{ m} \times 6 \text{ m}$ white rectangle shown in (a), averaged into $4 \text{ m} \times 6 \text{ m}$ bins (along \times across), with dotted lines showing $\pm 1\sigma$.

of the of the runway). After binning the overlapping data into 100 regions of $4 \text{ m} \times 6 \text{ m}$ (along \times across), the average RMS vertical difference from the local mean is 8.6 cm —comparable to the vertical RMS differences in recent airborne scanning lidar studies (Reineman et al. 2009). This calculation includes the inaccuracies from the measured laser range, the DGPS position, and offsets from attitude uncertainties. It is also influenced by the heterogeneity and slope of the surface within a binning region.

Imagery from the Manta Radiometric payload was collected at 5 Hz and is georeferenced using position data from the Novatel DGPS and attitude from the autopilot's IMU. After correcting for lens distortion, we project each image into an Earth reference frame using techniques described in Ma et al. (2004). The height of the UAV above the local ground (required for georeferencing) is derived using the lidar topographic data from the Flux payload, which are interpolated into a 2D digital elevation model of the region and then reinterpolated along the flight track of the UAV with the camera. The current georeferencing algorithm assumes a planar surface, optimized for ocean surface imagery.

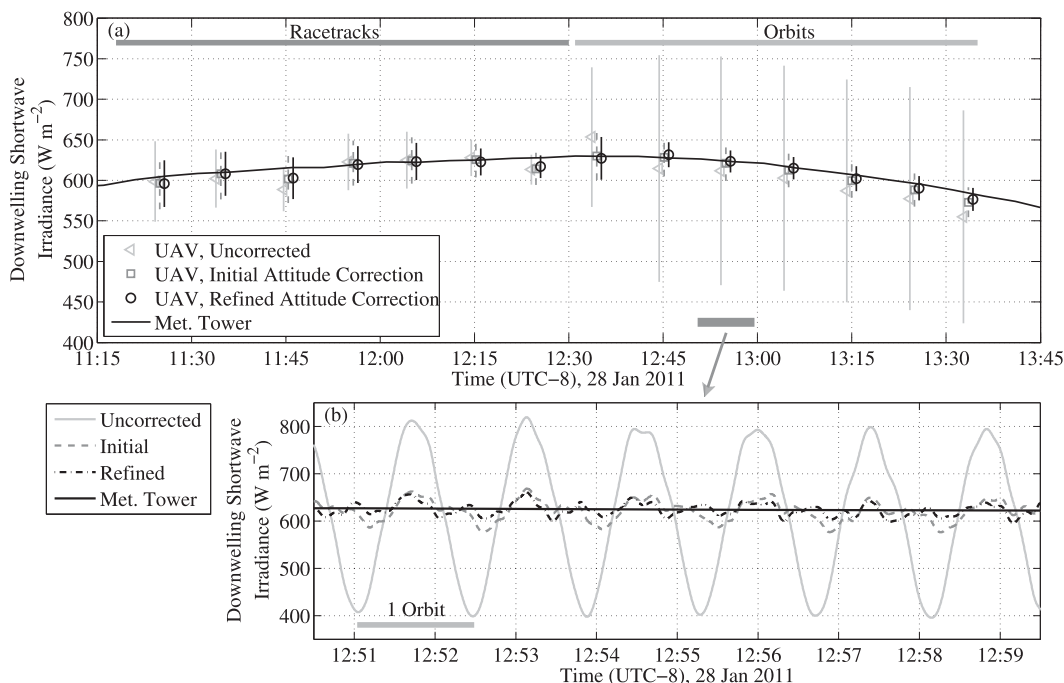


FIG. 15. (a) Time series of downwelling shortwave radiation, as measured with the Manta Radiometric payload and the CNR1 on the 13.5-m meteorological tower. There were clear-sky conditions, and the sun reached a maximum elevation of 36.2° at 1217 LT. Different symbols denote 10-min bin averages at different stages of the correction process (see section 4f), with vertical bars showing $\pm 1\sigma$ from the mean. Standard deviations are within 5% of the mean. Steep turns, ascents, and descents are not considered. First half of the data (1115–1230 LT) is obtained while the UAV is following a racetrack pattern over the runway, while the second (1230–1335 LT) is from repeated, constant-altitude orbits. UAV altitude was between 200 and 600 m AGL over the course of these measurements. During circular orbits, the roll is about 11° . (b) A 9-min subset of the time series, showing the measurements at different stages in the correction process before bin averaging.

f. Radiometric measurements and tower comparisons

Measurements of shortwave and longwave up- and downwelling radiation were obtained by the Radiometric Manta. Previous studies with UAV-based radiometric

measurements exist in the literature (e.g., Valero et al. 1996; Ramana et al. 2007), but details of the methods used in the present study are included for completeness.

We apply linear corrections, obtained by a stationary comparison with factory-calibrated radiometers (Campbell

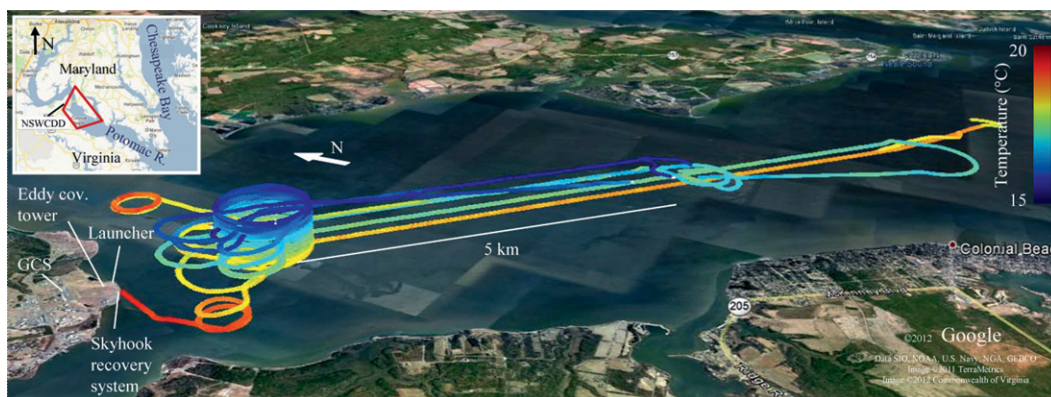


FIG. 16. Perspective view of flight track of ScanEagle with Flux payload over a section of the Potomac River on 13 Apr 2012, 1220–1420 EDT. Color scale corresponds to measured atmospheric temperature. Lowest two straight-and-level passes were 31 m above the surface, with other passes at 150, 300, and 460 m. ScanEagles were launched and recovered from NSWCCD.

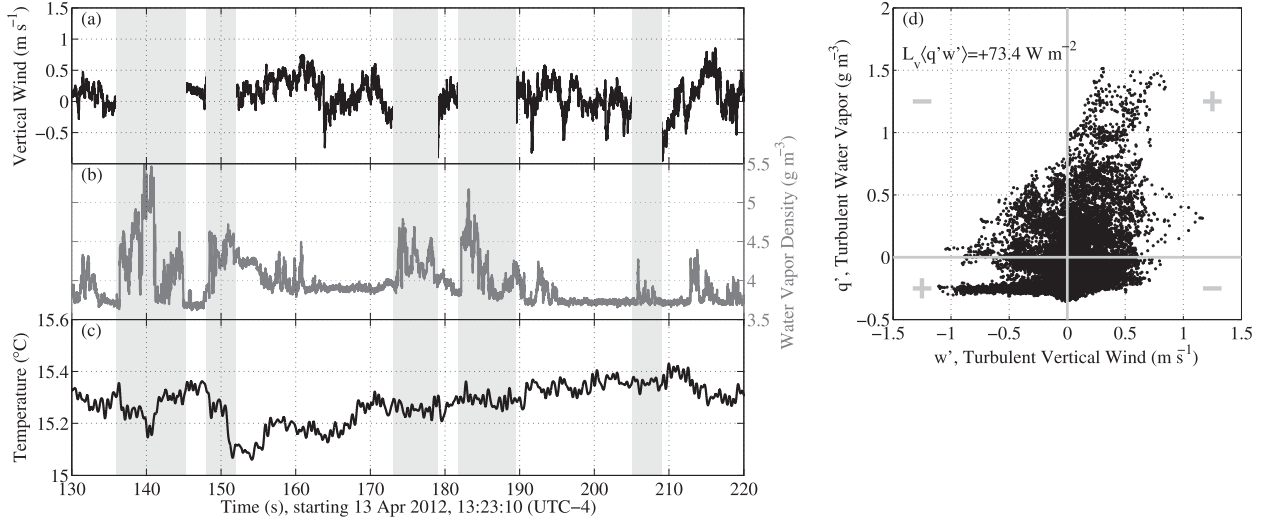


FIG. 17. Sample time series of variables measured by the ScanEagle Flux payload, at an altitude of 32.4 ± 3.1 m AGL over the Potomac River on 13 Apr 2012, showing (a) vertical wind; (b) water vapor concentration, as measured by the krypton hygrometer; and (c) temperature, as measured by the optical sensor (low-pass filtered with a 4-Hz-cutoff Butterworth filter). Positive correlation between vapor concentration and vertical wind can be seen (most notably in the times outlined in gray rectangles), implying positive vertical transport of water vapor and therefore positive latent heat. (d) Scatterplot of turbulent water vapor against turbulent vertical wind. Turbulent vapor flux can be calculated with the mean of the products of these quantities; shown is that calculated from the 90-s segment shown in (a)–(c). Plus and minus symbols show the sign of contribution to the flux within each quadrant. Water vapor flux is also quantified using integrated cospectra in Fig. 18b (see section 4c). Correlation between temperature and vertical wind is less pronounced, corresponding to the small and variable fluxes seen in Fig. 18c.

Scientific CNR1), to the measurements in order to remove any offsets added by the UAV's radiometer amplification circuit and analog-to-digital electronics. Aircraft pyranometers for downwelling measurements require special

treatment to account for nonlevel flight. We then determine the scaling factor S , applied to the measured downwelling shortwave radiation, $Q_{SW\downarrow, \text{corrected}} = S Q_{SW\downarrow, \text{measured}}$ (see, e.g., Bannehr and Glover 1991), given by

$$S = \frac{\sin \theta_s}{\cos \theta_s \sin \phi \sin(\psi_s - \psi) - \cos \theta_s \sin \theta \cos(\psi_s - \psi) + \sin \theta_s \cos \theta \cos \phi}, \quad (17)$$

where θ_s is the solar altitude (degrees above horizon), ψ_s is the azimuthal angle of the sun, ϕ is the aircraft roll, θ is pitch, and ψ is heading. Local solar position is calculated based on an algorithm by Reda and Andreas (2008). Given the clear-sky conditions during the flights, we assume for this correction that all the downwelling shortwave radiation is direct (i.e., none from Rayleigh scattering). For more detailed correction methods for airborne radiation measurements in partly cloudy conditions (not observed in the present experiment), we refer the reader to Boers et al. (1998).

To refine the scaling factor, we determine the angular offsets between the pyranometer and the IMU. As with the in-flight calibration refinement of the turbulence probe (section 4a), we first use a brute force and then a nonlinear optimization routine to determine

the pitch and roll combination that minimizes the RMS scatter about the 5-min running mean in the downwelling shortwave radiation within level circular orbits. With this technique, we determined offsets of -0.9° in pitch and -1.0° in roll in the present experiment, which are applied to the aircraft pitch and roll in the final downwelling shortwave radiation calculation. In Fig. 15, we compare a sample time series of downwelling shortwave radiation measured by the meteorological tower with radiation measured by the UAV, at various stages of the correction algorithm. The RMS difference between UAV- and tower-based 10-min bin-averaged downwelling shortwave radiation, after attitude corrections and incorporation of angular offsets, is 5.8 W m^{-2} (1.0%), down from 16.1 W m^{-2} (2.7%) before any correction and 7.2 W m^{-2} (1.2%) before final attitude refinement.

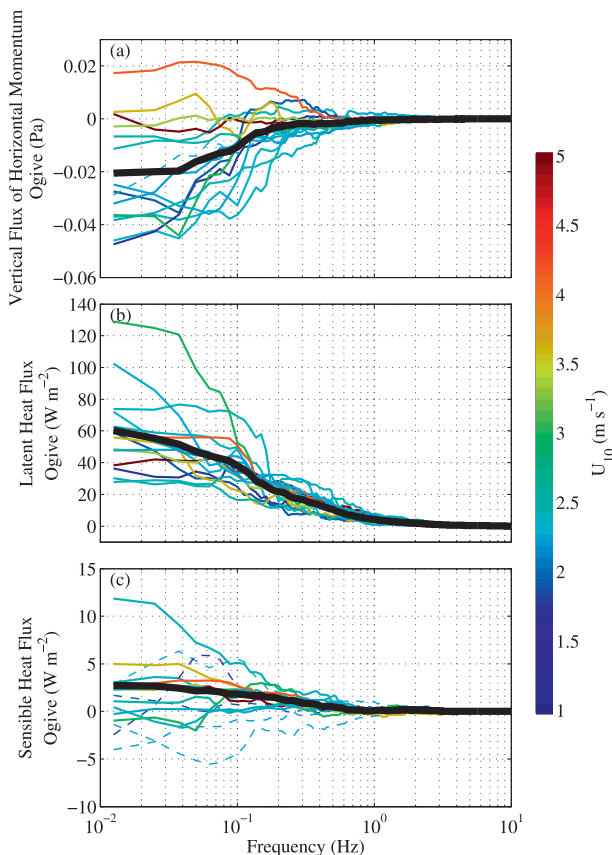


FIG. 18. Sample ogives from low-altitude passes (31.2 ± 4.6 m AGL) showing (a) vertical flux of horizontal momentum $\rho\langle u'w' \rangle$, (b) latent heat, and (c) sensible heat. To calculate these curves, cospectra are computed from sixteen 80-s segments (with 50% overlap), and then each is integrated from 10 Hz (4 Hz for sensible heat) to 0.013 Hz (80 s). Curves asymptotically approach the covariance, with the scalings noted in Eqs. (10)–(13). Most energy is seen in the range of 0.04–2 Hz, corresponding to length scales of 14–700 m, assuming a UAV airspeed of 28 m s^{-1} . Dotted ogives do not meet the quality control standards discussed in the text, and are not included in the means (solid black lines). Color scale is the 10-m wind speed (see text).

The quality of these measurements is limited when the response time of the instruments (provided by the manufacturer as 63% response at 6 s, the e -folding scale) is slow compared to the time scales of the UAV motion.² To mitigate this issue, measurements surrounding sharp turns ($>17^\circ$ in roll) and steep ascents and descents ($>5^\circ$ or $<-1^\circ$ in pitch) are neglected in the above-mentioned analysis. Before solar angle scaling

² High-quality pyranometers and pyrgeometers with faster responses (<1 s) are now commercially available, and will be incorporated into future versions of the payloads and discussed in future manuscripts.

corrections are applied, radiometer and attitude measurements are low-pass filtered with a cutoff frequency of $\frac{1}{6}$ Hz. After corrections, standard deviations within the binned measurements are $<5\%$ (see Fig. 15), which is within the 10% accuracy given by the radiometer manufacturer.

5. Engineering flight tests over water

Payloads aboard Boeing Insitu ScanEagles were tested with overwater flights at the Naval Surface Warfare Center, Dahlgren Division (NSWCDD, Dahlgren, Virginia; 38.3260°N , 77.0224°W), 12–16 April 2012. (A short video showing the ground equipment, launch, flight, and recovery during NSWCDD flight tests can be found at <http://airsea.ucsd.edu> under “Projects.”) NSWCDD controls an airspace (test range) of approximately $20 \text{ km} \times 5 \text{ km}$ horizontally and up to 600 m AGL over the Potomac River, where commercial ship and air traffic is restricted and UAV flights can be arranged. A short (1–2 h) flight was conducted for each payload (Flux, Radiometric, and Imaging). The flights were intended mainly as engineering tests, and successfully demonstrated 1) the scientific payloads could withstand the launch and recovery accelerations (measured up to 27 g), 2) real-time communication of scientific data and payload status to the ground control station (GCS), and 3) direct measurement of momentum and sensible and latent heat fluxes from low-altitude (down to 30 m) flights over water. The track of the Flux payload flight is presented in Fig. 16, as are positions of the GCS, pneumatic launcher, and SkyHook recovery system (see Figs. 2b and 2c). Eddy covariance instrumentation was installed on a 10-m tower in the same configuration as at McMillan Airfield (refer to Fig. 9e). Many of the analysis methods are similar to those described in section 4, though data are collected with redesigned payloads on different platforms. This section gives an overview of the flight tests and presents a brief description of results.

With the turbulence-probe-equipped Flux payload, we performed two 9-km straight-and-level passes at 30–32 m AGL, as well as several 5- and 9-km passes at 150, 300, and 460 m AGL and several vertical helical profiles up to 580 m AGL. Five reverse-pass pairs were used to refine the turbulence probe calibration using the methods described in section 4a. A sample time series of vertical wind, water vapor density, and temperature from the low-altitude flight legs are presented in Fig. 17. A correlation between vertical wind and water vapor density can be seen in the time series: positive vertical wind often coincides with higher vapor concentration, implying positive net vapor transport and thus positive

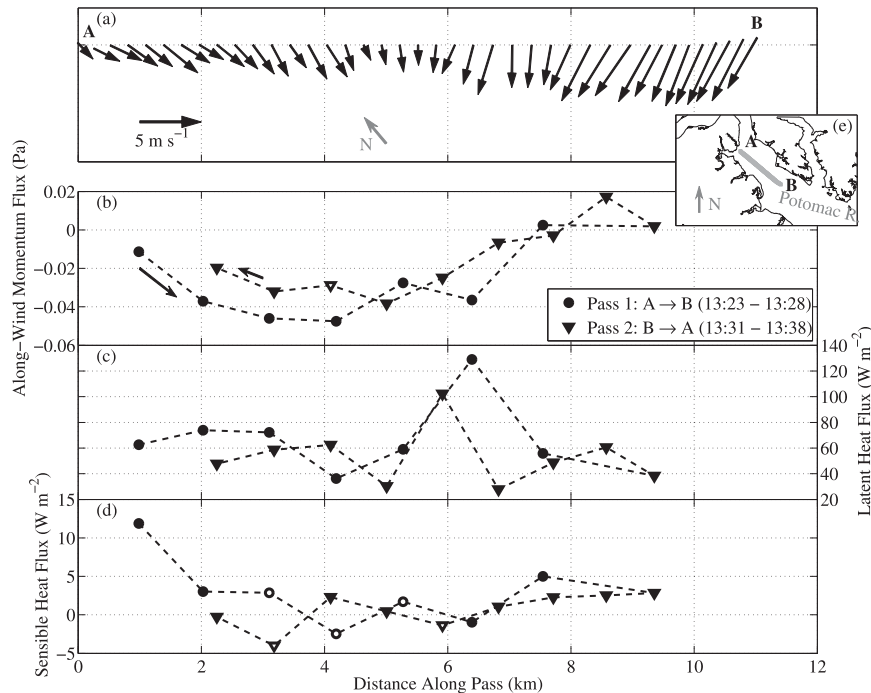


FIG. 19. (a) Low-altitude (31-m) flight track with measured horizontal wind vectors (pointing downwind) at 10-s intervals. (b) Vertical flux of along-wind horizontal momentum τ_x , (c) latent heat flux, and (d) sensible heat flux for the two passes, calculated with the integrated cospectra shown in Fig. 18. Data with hollow markers did not meet the quality control criteria (see text). A trend of more positive τ_x is observed toward the southeastern (down river) region in both pass directions, associated with an increase in wind speed and a shift in wind direction. Local start times (LT = UTC - 4 h) are given. (e) Map inset, showing the location of the 9-km segments as a thick gray line.

latent heat flux. Distinct bursts of moisture punctuate the near-constant background level (Fig. 17b).

Integrated cospectra (ogives) used to calculate momentum flux and sensible and latent heat flux are presented in Fig. 18. To calculate these curves, cospectra of vertical wind and the horizontal along-wind component, water vapor density, and virtual potential temperature, with the scalings noted in Eqs. (10)–(13), are computed, and then each is integrated from 10 Hz (4 Hz for sensible heat) to 0.013 Hz (80 s). Most energy is seen in the range of 0.04–2 Hz, corresponding to length scales of 14–700 m, assuming a UAV airspeed of 28 m s⁻¹. Each measurement is equivalent to a fixed-point measurement of 10–15 min given the wind speeds of 3–4 m s⁻¹, which is a reasonable averaging length for tower-based flux calculations (Friehe et al. 1991), though this is dependent on atmospheric stability—it can be longer for unstable and neutral conditions. The flux measurements are quality controlled by only accepting the measurement if the covariance above 0.05 Hz (20 s) is within 50% of the total covariance. This has the effect of excluding segments where unresolved large-scale coherent features are influencing the covariances (see,

e.g., French et al. 2007). Measurements with near-zero fluxes are also included. Rejected curves are denoted with dotted lines, and are not included in the mean. Figure 19 presents these fluxes as a function of along-track distance. A noticeable trend toward more positive vertical flux of along-wind momentum is observed toward the southeastern (down river) regions of the low-altitude passes, where wind has increased and shifted from northerly to more easterly (cross track). A significant increase in vapor flux (latent heat) is observed near the center of the segment, and is persistent in both pass directions.

With friction velocity computed as $u_* = (\langle u'w' \rangle^2 + \langle v'w' \rangle^2)^{1/4}$, the drag coefficient $C_D = (u_*/U_{10})^2$, ranges from 1.5×10^{-3} to 3.6×10^{-3} (10-m wind speed U_{10} is extrapolated from wind measured at the UAV altitude with Monin–Obukhov similarity theory; see, e.g., Jones and Toba 2001). This is in the range of other observations (Large and Pond 1981; Fairall et al. 2003; French et al. 2007), though more data over a wider range of conditions will be necessary to investigate relationships between C_D and wind speed and other environmental variables.

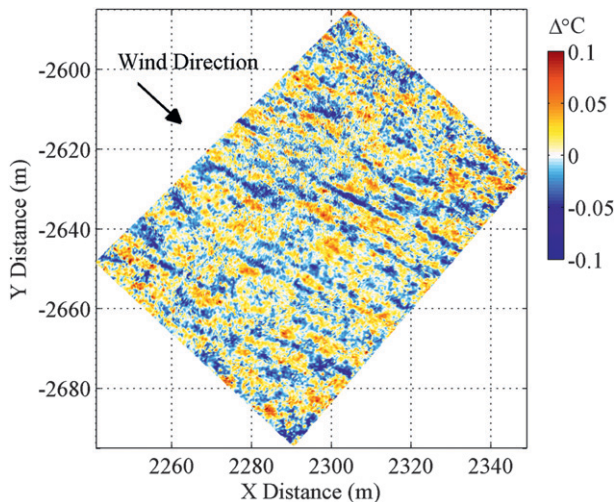


FIG. 20. Sample georeferenced infrared image obtained with the ScanEagle Imaging payload during flights over the Potomac River on 12 Apr 2012 from an altitude of 193 m AGL. Note the along-wind structures with a persistent 4–6-m spacing, indicative of Langmuir-type cells. Water depth in the vicinity of the image location is 2.5–3.0 m. Wind speed ($8.2 \pm 1.3 \text{ m s}^{-1}$, 1σ for ± 5 min surrounding time of image capture) and direction ($313^\circ \pm 14^\circ$) are calculated at the UAV altitude with the ScanEagle autopilot system based on heading, airspeed, and aircraft track.

Visible and infrared images captured by the ScanEagle Imaging payload are georeferenced using positioning and attitude data from the autopilot's DGPS/IMU, which is recorded at 5 Hz. Sample infrared imagery is presented in Fig. 20, showing an example of along-wind structures associated with Langmuir circulations. In convergence zones, water in the thin surface thermal boundary layer has had more exposure to the atmosphere, and appears cooler in the thermal imagery (Marmorino et al. 2005).

Lidar data from the ScanEagle Flux payload, georeferenced into Earth coordinates, give along-track profiles of the surface wave field over the Potomac River. At 31 m above the calm surface ($U_{10} = 2.3\text{--}4.1 \text{ m s}^{-1}$), we see a 93% signal return rate (this drops to 75% for 300-m passes). A boresight calibration was performed to determine the roll and pitch offsets that minimize the variance in surface elevation over calm water. Sample surface profile and wavenumber spectra are presented in Fig. 21. We have accounted for Doppler shift resulting from aircraft motion in the spectra (see Walsh et al. 1985; Hwang et al. 2000). The expected k^{-3} slope of the saturation spectra is shown for reference (Romero and Melville 2010).

6. Discussion

We have developed small unmanned aircraft instrument systems to measure momentum and energy

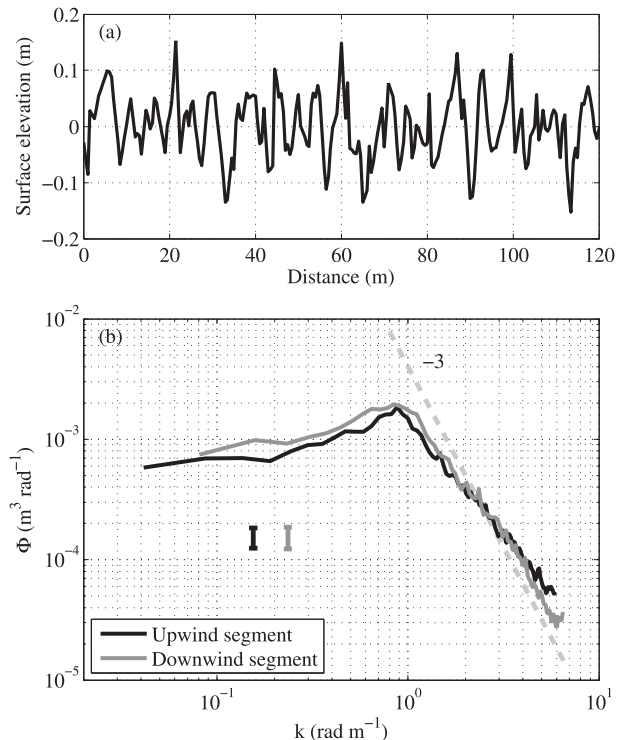


FIG. 21. (a) Sample surface wave field profile as measured by the ScanEagle Flux payload during low-altitude (30–32 m) passes over the Potomac River on 13 Apr 2012 (see Fig. 16). (b) Along-track wavenumber spectra, computed from two 9-km segments (one approximately upwind, one approximately downwind), split into 100-m Hanning windows with 50% overlap. Vertical bars indicate 95% confidence intervals. Spectra have been corrected to account for Doppler shifting associated with the aircraft speed relative to the wave speed. Both spectra peak at about 0.91 rad m^{-1} , corresponding to a wavelength of 6.9 m. Lidar data have been georeferenced into an Earth frame, with a boresight calibration applied to account for angular offsets between the IMU attitude and the lidar pointing direction (see text). A k^{-3} slope is shown for reference, representing the expected high-wavenumber saturation spectral slope.

fluxes within the atmospheric boundary layer. We have tested and verified instrumentation with ground-vehicle-based tests alongside research-standard instrumentation, with engineering flight tests over land and with low-altitude (down to 30 m) flight tests over water.

Coincident measurements of turbulent and radiative fluxes, topography, and multispectral imagery make this system a very useful tool for terrestrial atmospheric boundary layer research. For marine atmospheric boundary layer (MABL) research, topographic measurements and visible and infrared imagery of the sea surface will allow coincident observations of Langmuir cells, surface wave profiles, spectra and statistics, and wave breaking kinematics (Marmorino et al. 2005; Kleiss and Melville 2011). Measurements taken from within the MABL will permit

a more accurate determination of atmospheric state near the sea surface, and of the momentum flux (surface stress) and its relationship to the wind and surface wave field. These instrumented UAVs permit investigation of the spatial evolution of boundary layer fluxes and wave field kinematics, at altitudes considered unsafe for manned research aircraft.

Though fluxes have been measured from aircraft following approximately linear slant profiles (Mahrt 1985; Lenschow et al. 1988; Tjernström 1993), to the authors' knowledge, the present study is the first demonstration of measuring fluxes within precise vertical helical soundings, made possible in part because of the accuracy of the turbulence probe and DGPS/IMU. Many research opportunities arise because of the ability to measure vertical profiles of fluxes over a relatively small horizontal footprint: we can, for example, capture the evolution of the atmospheric boundary layer over transition zones such as air–sea ice boundaries or across sea surface temperature fronts. In the latter case, we would be able to simultaneously observe enhanced wave breaking that occurs at fronts due to wind–wave–current interactions (Melville 1996; Friehe et al. 1991; Baschek et al. 2006). We can also refine drag parameterizations and test the extent and validity of the constant flux layer assumption in a variety of conditions.

While similar measurements have been obtained from low-level manned aircraft and helicopter flights, the UAVs and instrument packages discussed here have the advantage of long-endurance and low-altitude flights at no risk to human pilots. Furthermore, with a 4.9-km service ceiling and up to 100-km line-of-sight communication range, the ship-based launch and recovery capability of an instrumented ScanEagle extends the reach of a research vessel and enables scientific measurements well beyond the immediate vicinity of the vessel. There is limited availability of long-range-capable research aircraft, but with ship-launched UAVs, measurements need no longer be restricted to coastal waters within the range of land-based manned (or unmanned) flight. UAV-based atmospheric and surface observations may also complement observations of surface and subsurface phenomena made from a vessel. Monitoring real-time atmospheric data from the UAVs will allow us to update flight patterns in real time in order to maximize coverage of phenomena of interest. Similarly, we can monitor patterns of atmospheric convection and precipitation with the vessel's weather radar, and direct flight paths to circumnavigate small [$O(10)$ km] and isolated convection structures, measuring horizontal wind velocities associated with lateral entrainment (e.g., Lenschow et al. 1999).

Interactions between the atmosphere and ocean at small scales have significant impacts on global circulation

and climate variability. Accurate in situ air–sea flux measurements in near-surface environments are essential for improving flux parameterizations, which not only underlie all satellite-derived air–sea flux products, but are also crucial for global climate projection models. Ultimately, instrumented UAVs such as those in this study will have an important role in collecting atmospheric measurements in extreme environments in support of improving air–sea flux products.

Acknowledgments. Daniel Bedenko was instrumental in assistance with electronics and integration (especially in the design of the sensor distribution circuitry in the ScanEagle payloads) and provided support with ground vehicle experiments. We thank Manta pilots Rafael Gaytan and Craig Baldwin for their support in the McMillan Airfield flights, and the Center for Interdisciplinary Remotely-Piloted Aircraft Studies (CIRPAS; Robert Bluth, Raymond Jackson, John Bendall) for providing McMillan Airfield ground support. We thank ScanEagle pilots and operators Lorenz Eber, Cyrus Roohi, Laura Bauer, Trevor Layh, and Adam Broad. We thank Joseph Katz, Gregory Morris, Peter Sutherland, and Nick Pizzo for their support with the SDSU wind tunnel experiments. Sutanu Sarkar shared valuable insight into the analysis of boundary layer data. We thank Ken Duff, Tom Maggard, and the SIO Marine Science Development Center for the machining of many components (including the turbulence probes) and for the pickup truck used in ground-vehicle-based experiments. This work was supported by grants to WKM from the Office of Naval Research (N00014-08-1-1024, N00014-11-1-0790, and N00014-11-1-0368). BDR was funded in part by a Jacobs Fellowship and grants from the California Space Grant Consortium at UCSD.

REFERENCES

- Bange, J., and R. Roth, 1999: Helicopter-borne flux measurements in the nocturnal boundary layer over land—A case study. *Bound.-Layer Meteor.*, **92**, 295–325.
- Bannehr, L., and V. Glover, 1991: Preprocessing of airborne pyranometer data. NCAR Tech. Note NCAR/TN-364+STR, 35 pp.
- Banta, R. M., Y. L. Pichugina, and W. A. Brewer, 2006: Turbulent velocity-variance profiles in the stable boundary layer generated by a nocturnal low-level jet. *J. Atmos. Sci.*, **63**, 2700–2719.
- Baschek, B., D. Farmer, and C. Garrett, 2006: Tidal fronts and their role in air-sea gas exchange. *J. Mar. Res.*, **64**, 483–515.
- Beardsley, R. C., A. G. Enriquez, C. A. Friehe, and C. A. Alessi, 1997: Intercomparison of aircraft and buoy measurements of wind and wind stress during SMILE. *J. Atmos. Oceanic Technol.*, **14**, 989–977.
- Blackadar, A. K., 1957: Boundary layer wind maxima and their significance for the growth of nocturnal inversions. *Bull. Amer. Meteor. Soc.*, **38**, 283–290.

- Boers, R., R. M. Mitchell, and P. B. Krummel, 1998: Correction of aircraft pyranometer measurements for diffuse radiance and alignment errors. *J. Geophys. Res.*, **103** (D13), 16753–16758.
- Bourassa, M. A., and Coauthors, 2013: High-latitude ocean and sea ice surface fluxes: Challenges for climate research. *Bull. Amer. Meteor. Soc.*, **94**, 403–423.
- Bradley, F., and C. Fairall, 2006: A guide to making climate quality meteorological and flux measurements at sea. NOAA Tech. Memo. OAR PSD-311, 107 pp.
- Brown, E. N., C. A. Friehe, and D. H. Lenschow, 1983: The use of pressure fluctuations on the nose of an aircraft for measuring air motion. *J. Climate Appl. Meteor.*, **22**, 171–180.
- Brunke, M. A., Z. Wang, X. Zeng, M. Bosilovich, and C.-L. Shie, 2011: An assessment of the uncertainties in ocean surface turbulent fluxes in 11 reanalysis, satellite-derived, and combined global datasets. *J. Climate*, **24**, 5469–5493.
- Cascella, G., J. J. Cione, E. W. Uhlhorn, and S. J. Majumdar, 2008: Inner-core characteristics of Ophelia (2005) and Noel (2007) as revealed by Aerosonde data. Preprints, *28th Conf. on Hurricanes and Tropical Meteorology*, Orlando, FL, Amer. Meteor. Soc., 7C4. [Available online at https://ams.confex.com/ams/28Hurricanes/techprogram/paper_137864.htm.]
- Cassano, J., and S. Knuth, 2010: UAV observations of the winter-time boundary layer over the Terra Bay Polynya, Antarctica. *Geophysical Research Abstracts*, Vol. 12, Abstract EGU2010-3619. [Available online at <http://meetingorganizer.copernicus.org/EGU2010/EGU2010-3619.pdf>.]
- Crawford, T. L., and R. J. Dobosy, 1992: A sensitive fast-response probe to measure turbulence and heat flux from any airplane. *Bound.-Layer Meteor.*, **59**, 257–278.
- Curry, J. A., and Coauthors, 2004: Seaflux. *Bull. Amer. Meteor. Soc.*, **85**, 409–424.
- Edson, J. B., A. A. Hinton, K. E. Prada, J. E. Hare, and C. W. Fairall, 1998: Direct covariance flux estimates from mobile platforms at sea. *J. Atmos. Oceanic Technol.*, **15**, 547–562.
- Enriquez, A. G., and C. A. Friehe, 1995: Effects of wind stress and wind stress curl variability on coastal upwelling. *J. Phys. Oceanogr.*, **25**, 1651–1671.
- Esposito, M., 2008: The operation, maintenance and calibration of turbulent wind sensing systems on research aircraft. Second Turbulence Expert Working Group meeting, Meeting Rep., Issue 1, ESA ESTEC, 65 pp. [Available online at <http://www.eufar.net/document/meeting/118164703548e9375526bf6:sue01.pdf>.]
- Fairall, C., E. Bradley, J. E. Hare, A. A. Grachev, and J. Edson, 2003: Bulk parameterization of air-sea fluxes: Updates and verification for the COARE algorithm. *J. Climate*, **16**, 571–591.
- French, J. R., W. M. Drennan, J. A. Zhang, and P. G. Black, 2007: Turbulent fluxes in the hurricane boundary layer. Part I: Momentum flux. *J. Atmos. Sci.*, **64**, 1089–1102.
- Friehe, C. A., and Coauthors, 1991: Air-sea fluxes and surface layer turbulence around a sea surface temperature front. *J. Geophys. Res.*, **96** (C5), 8593–8609.
- Garman, K. E., and Coauthors, 2006: An airborne and wind tunnel evaluation of a wind turbulence measurement system for aircraft-based flux measurements. *J. Atmos. Oceanic Technol.*, **23**, 1696–1708.
- Graber, H., E. Terray, M. Donelan, W. M. Drennan, J. C. van Leer, and D. B. Peters, 2000: ASIS—New Air-Sea Interaction Spar buoy: Design and performance at sea. *J. Atmos. Oceanic Technol.*, **17**, 708–720.
- Grachev, A. A., C. W. Fairall, J. E. Hare, J. B. Edson, and S. D. Miller, 2003: Wind stress vector over ocean waves. *J. Phys. Oceanogr.*, **33**, 2408–2429.
- Holder, H. E., M. A. Bolch, and R. Avissar, 2011: Processing turbulence data collected on board the Helicopter Observation Platform (HOP) with the empirical mode decomposition (EMD) method. *J. Atmos. Oceanic Technol.*, **28**, 671–683.
- Houston, A. L., B. Argrow, J. Elston, J. Lahowetz, E. W. Frew, and P. C. Kennedy, 2012: The Collaborative Colorado–Nebraska Unmanned Aircraft System Experiment. *Bull. Amer. Meteor. Soc.*, **93**, 39–54.
- Hwang, P. A., D. W. Wang, E. J. Walsh, W. B. Krabill, and R. N. Swift, 2000: Airborne measurements of the wavenumber spectra of ocean surface waves. Part I: Spectral slope and dimensionless spectral coefficient. *J. Phys. Oceanogr.*, **30**, 2754–2767.
- Jones, I. S. F., and Y. Toba, 2001: *Wind Stress over the Ocean*. Cambridge University Press, 326 pp.
- Kalogiros, J. A., and Q. Wang, 2002: Calibration of a radome-differential GPS system on a Twin Otter research aircraft for turbulence measurements. *J. Atmos. Oceanic Technol.*, **19**, 159–171.
- Katsaros, K. B., 1990: Parameterization schemes and models for estimating the surface radiation budget. *Surface Waves and Fluxes: Remote Sensing*, G. L. Geernaert and W. L. Plant, Eds., Environmental Fluid Mechanics, Vol. 2, Kluwer Academic Publishers, 339–368.
- Khelif, D., S. Burns, and C. Friehe, 1999: Improved wind measurements on research aircraft. *J. Atmos. Oceanic Technol.*, **16**, 860–875.
- Kleiss, J. M., and W. K. Melville, 2011: The analysis of sea surface imagery for whitecap kinematics. *J. Atmos. Oceanic Technol.*, **28**, 219–243.
- Lagarias, J. C., J. A. Reeds, M. H. Wright, and P. E. Wright, 1998: Convergence properties of the Nelder–Mead simplex method in low dimensions. *SIAM J. Optim.*, **9**, 112–147.
- Large, W. G., and S. Pond, 1981: Open ocean momentum flux measurements in moderate to strong winds. *J. Phys. Oceanogr.*, **11**, 324–336.
- Lenschow, D. H., 1986: Aircraft measurements in the boundary layer. *Probing the Atmospheric Boundary Layer*, D. H. Lenschow, Ed., Amer. Meteor. Soc., 39–55.
- , X. S. Li, C. J. Zhu, and B. B. Stankov, 1988: The stably stratified boundary layer over the Great Plains. *Bound.-Layer Meteor.*, **42**, 95–121.
- , P. Krummel, and S. Siems, 1999: Measuring entrainment, divergence, and vorticity on the mesoscale from aircraft. *J. Atmos. Oceanic Technol.*, **16**, 1384–1400.
- Lin, P.-H., and C.-S. Lee, 2008: The eyewall-penetration reconnaissance observation of Typhoon Longwang (2005) with unmanned aerial vehicle, Aerosonde. *J. Atmos. Oceanic Technol.*, **25**, 15–25.
- Ma, Y., S. Soatto, J. Kosecka, and S. S. Sastry, 2004: *An Invitation to 3-D Vision*. Springer-Verlag, 527 pp.
- Mahrt, L., 1985: Vertical structure and turbulence in the very stable boundary layer. *J. Atmos. Sci.*, **42**, 2333–2349.
- Marmorino, G., G. Smith, and G. Lindemann, 2005: Infrared imagery of large-aspect-ratio Langmuir circulation. *Cont. Shelf Res.*, **25**, 1–6.
- , B. Holt, M. J. Molemaker, P. M. DiGiacomo, and M. A. Sletten, 2010: Airborne synthetic aperture radar observations of “spiral eddy” slick patterns in the Southern California Bight. *J. Geophys. Res.*, **115**, C05010, doi:10.1029/2009JC005863.

- Martz, T. R., M. D. DeGrandpre, P. G. Strutton, W. R. McGillis, and W. M. Drennan, 2009: Sea surface $p\text{CO}_2$ and carbon export during the Labrador Sea spring-summer bloom: An in situ mass balance approach. *J. Geophys. Res.*, **114**, C09008, doi:10.1029/2008JC005060.
- Melville, W. K., 1996: The role of surface-wave breaking in air-sea interaction. *Annu. Rev. Fluid Mech.*, **28**, 279–321.
- , and P. Matusov, 2002: Distribution of breaking waves at the ocean surface. *Nature*, **417**, 58–63.
- Petersen, G. N., and I. A. Renfrew, 2009: Aircraft-based observations of air-sea fluxes over Denmark Strait and the Irminger Sea during high wind speed conditions. *Quart. J. Roy. Meteor. Soc.*, **135**, 2030–2045.
- Pham, H., S. Sarkar, and K. Brucker, 2010: Dynamics of a stratified shear layer above a region of uniform stratification. *J. Fluid Mech.*, **630**, 191–223.
- Pope, S. B., 2000: *Turbulent Flows*. Cambridge University Press, 771 pp.
- Ramana, M. V., V. Ramanathan, D. Kim, G. C. Roberts, and C. E. Corrigan, 2007: Albedo, atmospheric solar absorption and heating rate measurements with stacked UAVs. *Quart. J. Roy. Meteor. Soc.*, **133**, 1913–1931.
- Reda, I., and A. Andreas, 2008: Solar position algorithm for solar radiation applications. National Renewable Energy Laboratory Tech. Rep. NREL/TP-560-34302, 39 pp.
- Reineman, B. D., L. Lenain, D. Castel, and W. K. Melville, 2009: A portable airborne scanning lidar system for ocean and coastal applications. *J. Atmos. Oceanic Technol.*, **26**, 2626–2641.
- Romero, L., and W. K. Melville, 2010: Airborne observations of fetch-limited waves in the Gulf of Tehuantepec. *J. Phys. Oceanogr.*, **40**, 441–465.
- Taylor, J., and S. Sarkar, 2008: Stratification effects in a bottom Ekman layer. *J. Phys. Oceanogr.*, **38**, 2535–2555.
- Thomas, R., K. Lehmann, H. Nguyen, D. Jackson, D. Wolfe, and V. Ramanathan, 2012: Measurement of turbulent water vapor fluxes using a lightweight unmanned aerial vehicle system. *Atmos. Meas. Tech.*, **5**, 243–257.
- Tjernström, M., 1993: Turbulence length scales in stably stratified free shear flow analyzed from slant aircraft profiles. *J. Appl. Meteor.*, **32**, 948–963.
- Turner, J., 1973: *Buoyancy Effects in Fluids*. Cambridge University Press, 367 pp.
- Valero, F. P. J., S. K. Pope, R. G. Ellingson, A. W. Strawa, and J. Vitko Jr., 1996: Determination of clear-sky radiative flux profiles, heating rates, and optical depths using unmanned aerospace vehicles as a platform. *J. Atmos. Oceanic Technol.*, **13**, 1024–1030.
- Van den Kroonenberg, A., T. Martin, M. Buschmann, J. Bange, and P. Vörsmann, 2008: Measuring the wind vector using the autonomous mini aerial vehicle M²AV. *J. Atmos. Oceanic Technol.*, **25**, 1969–1982.
- Vickers, D., and L. Mahrt, 1997: Quality control and flux sampling problems for tower and aircraft data. *J. Atmos. Oceanic Technol.*, **14**, 512–526.
- Walsh, E. J., D. W. Hancock, D. E. Hines, R. N. Swift, and J. F. Scott, 1985: Directional wave spectra measured with the surface contour radar. *J. Phys. Oceanogr.*, **15**, 566–592.
- Webster, P., and R. Lukas, 1992: TOGA COARE: The coupled ocean–atmosphere response experiment. *Bull. Amer. Meteor. Soc.*, **73**, 1377–1416.
- Williams, A., and D. Marcotte, 2000: Wind measurements on a maneuvering twin-engine turboprop aircraft accounting for flow distortion. *J. Atmos. Oceanic Technol.*, **17**, 795–810.
- Yelland, M., B. Moat, P. Taylor, R. Pascal, J. Hutchings, and V. Cornell, 1998: Wind stress measurements from the open ocean corrected for airflow distortion by the ship. *J. Phys. Oceanogr.*, **28**, 1511–1526.
- Young, I., 1995: The determination of confidence limits associated with estimates of the spectral peak frequency. *Ocean Eng.*, **22**, 669–686.

CORRIGENDUM

BENJAMIN D. REINEMAN

*Scripps Institution of Oceanography, and Department of Mechanical and Aerospace Engineering,
University of California, San Diego, La Jolla, California*

LUC LENAIN, NICHOLAS M. STATOM, AND W. KENDALL MELVILLE

Scripps Institution of Oceanography, University of California, San Diego, La Jolla, California

In the final processing of Reineman et al. (2013), the appearance of Fig. 17 on p. 1313 was inadvertently altered. Figure 17 appears below as it was meant to be shown.

The staff of the *Journal of Atmospheric and Oceanic Technology* regrets any inconvenience this error may have caused.

REFERENCE

Reineman, B. D., L. Lenain, N. M. Statom, and W. K. Melville, 2013: Development and testing of instrumentation for UAV-based flux measurements within terrestrial and marine atmospheric boundary layers. *J. Atmos. Oceanic Technol.*, **30**, 1295–1319.

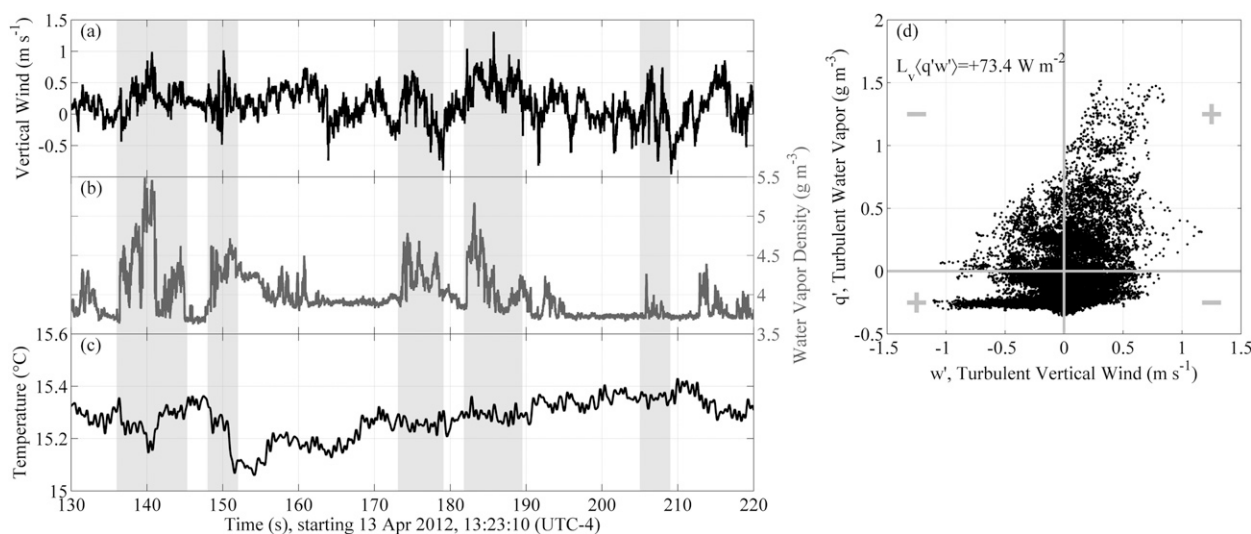


FIG. 17. Sample time series of variables measured by the ScanEagle Flux payload, at an altitude of $32.4 \pm 3.1 \text{ m}$ AGL over the Potomac River on 13 Apr 2012, showing (a) vertical wind; (b) water vapor concentration, as measured by the krypton hygrometer; and (c) temperature, as measured by the optical sensor (low-pass filtered with a 4-Hz-cutoff Butterworth filter). Positive correlation between vapor concentration and vertical wind can be seen (most notably in the times outlined in gray rectangles), implying positive vertical transport of water vapor and therefore positive latent heat. (d) Scatterplot of turbulent water vapor against turbulent vertical wind. Turbulent vapor flux can be calculated with the mean of the products of these quantities; shown is that calculated from the 90-s segment shown in (a)–(c). Plus and minus symbols show the sign of contribution to the flux within each quadrant. Water vapor flux is also quantified using integrated cospectra in Fig. 18b (see section 4c). Correlation between temperature and vertical wind is less pronounced, corresponding to the small and variable fluxes seen in Fig. 18c.